Full Title

Non-autonomous insulin signaling regulates the duration of mitosis in *C. elegans* germline stem and progenitor cells

Short Title

Stem cell mitosis in vivo and its regulation by signaling pathways

Eric Cheng[1], Ran Lu[1] and Abigail R. Gerhold[1]

[1] Department of Biology, McGill University, 1205 avenue Docteur Penfield, Montréal, QC, H2A 1B1, Canada.

Corresponding author: Abigail Gerhold (abigail.gerhold@mcgill.ca)

Abstract

Stem and progenitor cell mitosis is essential for tissue development and homeostasis. How these cells ensure proper chromosome segregation, and thereby maintain mitotic fidelity, in the complex physiological environment of a living animal is poorly understood. Here we use *in situ* live-cell imaging of *C. elegans* germline stem and progenitor cells (GSPCs) to ask whether signaling pathways that play a conserved role in regulating stem and progenitor cell cycle progression also impact mitosis. Through a candidate screen we identify a new role for the insulin/IGF receptor (IGFR), *daf-2,* as a regulator of GSPC mitosis. Mitosis is delayed in *daf-2/*IGFR mutants, and these delays require canonical, DAF-2/IGFR to DAF-16/FoxO insulin signaling, here acting cell non-autonomously from the soma. We further show that while mitotic delays in *daf-2*/IGFR mutants depend on the spindle assembly checkpoint, they are not accompanied by a loss of mitotic fidelity. Finally, we show that caloric restriction, which delays GSPC mitosis and compromises mitotic fidelity, does not act via the canonical insulin signaling pathway, and instead requires AMP-activated kinase (AMPK). Together this work demonstrates that GSPC mitosis is regulated by at least two genetically separable signaling pathways and highlights the importance of signaling networks for proper stem and progenitor cell mitosis *in vivo*.

Author Summary

Stem and progenitor cells drive tissue development and sustain adult tissue turnover by producing new daughter cells via cell division and the success of cell division relies on proper chromosome segregation during mitosis. Stem and progenitor cells perform mitosis in the complex environment of a living animal, yet relatively little is known about how events during mitosis are influenced by this *in vivo* context. Here we took advantage of the germline stem and progenitor cells of the model nematode *C. elegans* to ask whether signaling pathways that coordinate stem and progenitor cell division with external cues also play a role during mitosis. We uncovered a role for the insulin signaling pathway in regulating mitosis in these cells. Reduced insulin signaling delays germline stem and progenitor cell mitosis without compromising chromosome segregation and acts non-autonomously from somatic tissues. While insulin signaling is known to link cell division with nutritional status in many species, we found that it did not mediate the effects of caloric restriction on germline stem and progenitor cell mitosis. Instead, caloric restriction acts via the conserved energy-sensing regulator AMPK. These results uncover new regulators of germline stem and progenitor cell mitosis and emphasize the importance of signaling pathways for proper stem and progenitor cell mitosis *in vivo*.

50 **Introduction**

51 The ability of stem and progenitor cells to support tissue development and homeostasis relies
52 on signaling networks to couple cell cycle progression with organismal physiology and
53 developmental cues. Signaling pathways ensure the appropriate production of daughter cells by
54 interacting with the core cell cycle machinery to control passage from the G1 to S and G2 to M
55 phases of the cell cycle (reviewed in (1)). Whether these same pathways also regulate events in
56 M phase, particularly those required for stem and progenitor cells to ensure proper chromosome
57 segregation in mitosis, and therefore genomic integrity, is less clear.

58 Error-free mitoses require that replicated chromosome pairs are attached to and bi-oriented
59 on the mitotic spindle, via stable kinetochore-microtubule attachments, prior to the onset of
60 chromosome segregation in anaphase. The spindle assembly checkpoint safeguards this process
61 by delaying anaphase in the presence of unattached kinetochores. Unattached kinetochores
62 recruit checkpoint proteins to catalyze formation of the mitotic checkpoint complex (MCC), which
63 prevents the anaphase-promoting complex/cyclosome (APC/C) from targeting mitotic
64 substrates, like cyclin B and Securin, for degradation (reviewed in (2)). Defects in spindle assembly
65 and/or checkpoint surveillance can lead to chromosome segregation errors, compromising
66 genomic stability and cellular fitness (3).

67 Signaling pathways can influence mitotic events directly or indirectly through changes in gene
68 expression. For example, in transformed human cells, hyperactive Ras/MAPK signaling leads to
69 excessive phosphorylation of kinetochore proteins and impaired kinetochore-microtubule
70 attachments (4), while changes in gene expression downstream of insulin signaling affect spindle
71 assembly and/or checkpoint activity in several cell types (5-8). However, much of the work linking

72 signaling pathways to mitotic events has been carried out in *ex vivo* model systems.
73 Consequently, how physiological changes in signaling pathway activity influence mitosis *in vivo*,
74 is not well understood, but likely important for stem and progenitor cells to maintain mitotic
75 fidelity within the changeable environment of a living organism.

76 The germline stem and progenitor cells (GSPCs) of the nematode *Caenorhabditis elegans* are
77 an established model for how stem and progenitor cells match their proliferative state with tissue
78 demand and animal physiology (9-15). *C. elegans* hermaphrodites have two pools of GSPCs, one
79 located at the distal tip of each of the two U-shaped gonad arms (**Fig 1A**; reviewed in (16)). GSPCs
80 are kept in an undifferentiated, mitotic state by proximity to a somatic niche, the distal tip cell.
81 Collectively, the distal region of the germ line is referred to as the progenitor or proliferative zone
82 (PZ) and comprises two populations of mitotically cycling germ cells - the distal-most cells with
83 the highest level of niche signaling are considered stem cells. These cells divide symmetrically
84 with respect to cell fate and are maintained according to a population-based model (17). The
85 more proximal cells are progenitor cells completing their final mitotic cell cycle before entering
86 meiosis. Meiotic germ cells can become nurse cells, eventually undergoing apoptosis, or give rise
87 to mature gametes, which are found at the proximal end of the gonad. Thus, proper GSPC
88 proliferation is intimately linked with reproduction and correspondingly under tight control by
89 both local and systemic cues.

90 GSPC mitosis can be observed directly by live-cell imaging in whole-mount animals (18-20),
91 making them an excellent model system for studying stem and progenitor cells mitosis *in vivo*.
92 We have shown previously that caloric restriction leads to checkpoint-dependent mitotic delays
93 in GSPCs and may perturb spindle assembly (18), supporting the idea that mitosis *in vivo* is

94 influenced by the physiological status of the whole animal. Here we report a candidate genetic
95 screen for signaling pathway mutants that impact mitotic duration in GSPCs and uncover a role
96 for the insulin/IGF receptor (IGFR) *daf-2* in promoting proper GSPC mitotic timing. We show that
97 DAF-2/IGFR acts via the canonical insulin/IGF-1 signaling (IIS) pathway, converging on the
98 transcription factor DAF-16/FoxO; however, the predominant site of pathway activity resides
99 outside of the germ line in the soma, and is thus cell non-autonomous. Surprisingly, we find that
100 while reduced IIS leads to checkpoint-dependent mitotic delays, it does not compromise mitotic
101 fidelity. This is different from caloric restriction, which we show increases the frequency of
102 chromosome segregation errors when surveillance by the spindle assembly checkpoint is
103 compromised. Correspondingly, we find different genetic requirements for mitotic delays
104 downstream of caloric restriction and reduced DAF-2/IGFR activity.
105
106 **Results**
107 *A candidate screen for signaling pathways that affect mitotic duration uncovers daf-2/IGFR*
108 Several conserved signaling pathways regulate GSPC fate (i.e. whether to remain mitotic or
109 enter meiosis) and/or cell cycle progression, both during development and in the adult animal
110 (**Fig 1B**; reviewed in (16, 21)). The Notch pathway regulates the mitosis-meiosis decision in GSPCs
111 (22), but does not affect cell cycle progression per se (23, 24). Transforming Growth Factor-β
112 (TGF-β) signaling acts both upstream of and in parallel to Notch signaling to regulate GSPC fate
113 (25, 26) and has also been implicated in the maintenance of GSPCs during reproductive aging
114 (27). The TOR pathway is thought to affect both GSPC fate and cell cycle progression (28, 29) and
115 plays a role in regulating GSPC quiescence during L1 larval and dauer diapause (30-32). Regulation

116 of GSPC quiescence in larvae and adults also requires AMP-activated kinase (AMPK) (10, 31, 33)
117 and the lipid and protein phosphatase PTEN, here acting independently of the transcription factor
118 FoxO (9-11, 30, 34, 35). Ras/MAPK pathway activity affects GSPC proliferation (33, 36, 37),
119 although its primary role in the germline is to promote meiotic progression and oocyte
120 maturation (36, 38, 39). Finally, the IIS pathway, via inhibition of FoxO, promotes GSPC
121 proliferation and is particularly important for larval expansion of the GSPC pool (11, 24, 40).

122 We crossed mutant alleles of key genes in each pathway into our reference strain, which
123 carries germline-expressed, GFP-tagged β-tubulin (GFP::TBB-2) to mark mitotic spindles and
124 mCherry-tagged histone H2B (mCH::HIS-11) to mark chromatin (**Fig 1C-D**). We focused our
125 analysis on the L4 larval stage of development (**Fig 1A**), as GSPCs proliferate extensively during
126 this time and may be more sensitive to changes in environmental and/or developmental signaling
127 (24, 28, 41).

128 We first scored the GSPC mitotic index in these strains, by counting the total number of PZ
129 nuclei and the total number of cells in mitosis (**Fig 1E and S1A-B Fig**). We found that reducing
130 insulin pathway activity via a hypomorphic allele of the insulin/IGF receptor (IGFR) *daf-2* (*daf-*
131 *2(e1370)* (42); hereafter *daf-2(rf)*) lead to a lower mitotic index, while all other conditions were
132 not significantly different from control, despite wide ranging alterations in the number of PZ
133 nuclei. This result aligns well with previous reports suggesting that the insulin pathway is the
134 chief regulator of GSPC cell cycle progression during larval development (24). The mitotic index
135 tended to be lower in animals carrying a hypomorphic allele of *daf-7*/TGF-β (*daf-7(e1320)*; (43)),
136 although this result was not statistically different from control (p = 0.09), suggesting that TGF-β
137 may also regulate GSPC proliferation. Our results differ from the literature in one regard: a loss-

138 of-function allele of ribosomal S6 kinase (S6K) *rsks-1* (*rsks-1(ok1255)* (44)), which acts
139 downstream of TOR in many species, and which has been shown to strongly reduce the number
140 PZ cells (28), had no effect in our hands (**S1A Fig**). We do not know what underlies this
141 discrepancy, but suspect that it could be due to genetic background and/or to gene-diet
142 interactions (45).

143 To determine whether these pathways affect GSPC mitosis, we performed live-cell imaging
144 and used GFP::TBB-2 to track pairs of mitotic spindle poles, which allows us to monitor mitotic
145 progression by looking for the stereotypical changes in spindle length that accompany mitotic
146 transitions (**Fig 1D**; (18-20)). We defined the duration of mitosis as the amount of time between
147 the end of NEBD, when spindle length stops decreasing, until the metaphase-anaphase
148 transition, after which spindle length increases rapidly. In GSPCs, the duration of mitosis is
149 dictated by the timing of anaphase onset and is regulated by the spindle assembly checkpoint,
150 with conditions that disrupt spindle assembly or weaken the checkpoint prolonging or reducing
151 mitotic duration, respectively (18). We found that GSPCs in animals bearing hypomorphic alleles
152 of *daf-2*/IGFR, *daf-7*/TGF-β or *glp-1*/Notch had significantly longer durations of mitosis, while
153 those in animals bearing a hypomorphic allele of *mpk-1*/ERK, gain-of-function alleles of *let-*
154 *60*/Ras or *glp-1*/Notch or null alleles of *daf-18*/PTEN, *rsks-1*/S6K and *aak-1/2*/AMPK divided with
155 timing similar to control (**Fig 1F**).

156 In addition to providing a measure of mitotic duration, spindle pole tracking allows us to
157 extract a range of mitotic features related to spindle assembly and/or chromosome alignment
158 and segregation (**S2A Fig**; (20)). When we compared mitotic features across all genotypes, we did
159 not observe any obvious trends that might explain changes in the duration of mitosis (**S2B Fig**).

160 Correspondingly, no features were strongly correlated with the duration of mitosis across all cells
161 (**S2C Fig**). To determine whether different genotypes and/or cells with longer durations of mitosis
162 (delayed cells) were defined by different combinations of features, we performed a principal
163 component analysis (PCA). While we did not observe any well-defined clusters within our data,
164 delayed cells in *daf-2(rf)* and *daf-7*/TGF-β hypomorphic animals tended to separate in PC space
165 from those in *glp-1*/Notch hypomorphic animals, suggesting that these cells are defined by
166 different combinations of mitotic features (**S2D Fig**). Altogether, our data implicate the IIS, TGF-
167 β and Notch pathways in the regulation of GSPC mitosis and suggest a degree of specificity in
168 how they impact spindle formation and/or dynamics.
169
170 *daf-2/IGFR regulates mitotic duration via the canonical IIS pathway*
171 To begin to decipher how different signaling pathway mutants affect GSPC mitosis, we
172 focused our attention on *daf-2(rf)* and the IIS pathway. DAF-2/IGFR activates a canonical
173 phosphoinositide 3-kinase (PI3K)/Akt signaling cascade, which is antagonized by DAF-18/PTEN,
174 to inhibit the Forkhead family transcription factor DAF-16/FoxO (**Fig 2A**). This core pathway is
175 conserved and plays a major role in integrating cell proliferation with organism physiology in
176 many species (reviewed in (46)).
177 In *C. elegans* GSPCs, *daf-2(rf)* mutants have fewer germ cells, and a lower mitotic index,
178 primarily due to a delay in the G2 phase of the cell cycle, and these effects are mediated by DAF-
179 16/FoxO (24). Correspondingly, we found that the low GSPC mitotic index in *daf-2(rf)* mutants
180 was suppressed by a catalytically dead allele of *daf-18*/PTEN (*daf-18(nr2037)* (47); hereafter *daf-*
181 *18(lf)*) and a dominant-activating allele of *akt-1* (*akt-1(mg144)* (48); hereafter *akt-1(gf)*), which

182 increase pathway activity downstream of DAF-2/IGFR, and by a null allele of *daf-16*/FoxO (*daf-*
183 *16(mu86)* (49); hereafter *daf-16(0)*), which simulates the transcriptional response induced by
184 high pathway activity (**S3A Fig,** (24)).

185 To test whether the canonical IIS pathway also mediates the effect of *daf-2(rf)* on the duration
186 of mitosis in GSPCs, we used live-cell imaging and spindle pole tracking to measure mitotic
187 duration in *daf-18(lf)*, *akt-1(gf)* and *daf-16(0)* single mutants and in double mutants carrying each
188 of these alleles with *daf-2(rf)* (**Fig 2B**). We found that the duration of mitosis was unchanged in
189 *daf-18(lf)*, *akt-1(gf)* and *daf-16(0)* single mutants, as compared to wild-type control, suggesting
190 that elevating IIS is not sufficient to accelerate basal mitotic timing; however, all three mutations
191 fully suppressed *daf-2(rf)* mitotic delays, indicating that reduced DAF-2/IGFR activity prolongs
192 GSPC mitosis via the canonical IIS pathway converging on the regulation of DAF-16/FoxO.

193 DAF-2/IGFR inhibits DAF-16/FoxO transcriptional activity by regulating its subcellular
194 localization: when DAF-2/IGFR is active, DAF-16/FoxO is sequestered in the cytoplasm (50-52).
195 Accordingly, if DAF-2/IGFR regulates GSPC mitosis via DAF-16/FoxO-dependent changes in gene
196 expression, we would expect increased DAF-16/FoxO nuclear localization in GSPCs when DAF-
197 2/IGFR activity is reduced. To test this, we measured the nuclear-to-cytoplasmic ratio of DAF-
198 16::GFP in GSPCs, using a strain in which the endogenous *daf-16*/FoxO locus bears a carboxyl-
199 terminal GFP tag to mark all isoforms (DAF-16::GFP; (53)) (**Fig 2C)**. We found that DAF-16::GFP
200 was enriched in GSPC nuclei in both *daf-2(rf)* animals (**Fig 2C-E**) and in animals in which *daf-2* was
201 depleted by RNAi (**S3B Fig**).

202 In *daf-2(rf)* animals, the duration of GSPC mitosis varies from ~5 minutes, which is similar to
203 the mean duration for controls, up to ~25 minutes (see **Figs 1F and 2B**). To determine whether

204 differences in DAF-16::GFP nuclear enrichment might account for this variation, we plotted the
205 DAF-16::GFP nuclear-to-cytoplasmic ratio prior to mitosis versus mitotic duration on a per cell
206 basis (**Fig 2F-G and S3C Fig**). However, we found only a weak, non-statistically significant,
207 correlation between these two values. Furthermore, nuclear DAF-16::GFP was elevated (nuclear-
208 to-cytoplasmic ratio > 1.4) even in *daf-2(rf)* GSPCs with relatively normal durations of mitosis (4-
209 6 min). Thus, while reducing the activity of DAF-2/IGFR leads to increased nuclear localization of
210 DAF-16/FoxO in GSPCs, nuclear enrichment of DAF-16/FoxO is unlikely to be the sole determinant
211 of mitotic delays.
212
213 *IIS regulates the duration of mitosis cell non-autonomously*
214 The lack of a predictive relationship between GSPC DAF-16/FoxO nuclear enrichment and
215 GSPC mitotic duration prompted us to ask whether DAF-2/IGFR to DAF-16/FoxO signal
216 transduction was acting in GSPCs (i.e. cell autonomously) to promote proper mitotic timing or
217 whether cell non-autonomous signaling might be involved. To test this idea directly, we used the
218 auxin-inducible degron (AID) system which allows for the conditional depletion of AID-tagged
219 proteins using tissue-specific expression of the F-box substrate recognition component TIR1 (54).
220 We used a strain in which the endogenous *daf-2*/IGFR locus is tagged at the carboxyl-terminus
221 with AID and mNeonGreen (DAF-2::AID::mNG; (55)). In the PZ of L4 larvae, DAF-2::AID::mNG
222 showed weak membrane localization, appearing largely as cytoplasmic puncta (**S4A Fig**).
223 We generated strains carrying DAF-2::AID::mNG and a germline-specific TIR1 (*sun1p::TIR1*;
224 (54)), with either mCherry-tagged β-tubulin (mCH::TBB-2) for spindle pole tracking, or DAF-
225 16::GFP. We found that depletion of DAF-2/IGFR in the germ line led to increased nuclear DAF-

226 16::GFP in GSPCs (**Fig 3A-C**), consistent with cell autonomous DAF-2/IGFR to DAF-16/FoxO
227 signaling. However, germline DAF-2/IGFR depletion did not delay GSPC mitosis (**Fig 3D**), further
228 suggesting that elevated nuclear DAF-16/FoxO in GSPCs is not sufficient to affect mitotic timing.
229 These results also imply that mitotic delays in *daf-2(rf)* animals may be due to a cell non-
230 autonomous requirement for DAF-2/IGFR activity. Correspondingly, depletion of *daf-2/IGFR*
231 using germline-specific RNAi (56) did not affect mitotic duration in GSPCs, whereas RNAi
232 depletion in the whole animal induced significant mitotic delays (**S4B Fig**).

233 To test whether reducing somatic DAF-2/IGFR activity was sufficient to delay GSPC mitosis,
234 we performed analogous experiments using a strain bearing pan-somatic TIR1 (*eft-3p::TIR1* with
235 the *unc-54* 3' UTR; (54)). In our hands, *eft-3p::TIR1* DAF-2::AID::mNG animals showed reduced
236 DAF-2::AID::mNG in somatic tissues and phenotypes consistent with a partial loss of DAF-2/IGFR
237 somatic activity even without supplemental auxin (**Fig 3A and S4C Fig**). However, germline
238 expression of DAF-2::AID::mNG and GSPC DAF-16::GFP nuclear localization were similar to what
239 we observed in our germline-specific TIR1, no auxin controls, suggesting that germline DAF-
240 2/IGFR activity was relatively intact (**Fig 3B-C**). We therefore took advantage of these animals to
241 test the effect of partial somatic DAF-2/IGFR depletion on GSPC mitosis and found that mitosis
242 was significantly delayed (**Fig 3D**). Together these results imply that the focus of DAF-2/IGFR
243 activity responsible for the duration of mitosis in GSPCs resides in the soma.

244 To determine whether DAF-16/FoxO also acts cell non-autonomously, we used the AID
245 system to deplete DAF-16/FoxO (DAF-16::GFP::AID; (55)) in the germ line (*sun-1p::TIR1*) or in the
246 soma (*eft-3p::TIR1*) and asked whether either was sufficient to suppress GSPC mitotic delays
247 induced by whole-animal RNAi knockdown of *daf-2*. In these experiments, *eft-3p::TIR1* induced

248 significant depletion of DAF-16::GFP::AID in both the soma and the germ line following auxin
249 treatment, while *sun-1p::TIR1*-driven depletion was restricted to the germ line as expected (**S4D**
250 **Fig**). However, auxin treatment only suppressed *daf-2*(RNAi)-induced GSPC mitotic delays in the
251 *eft-3p::TIR1* background (**Fig 3E**). Thus, while we cannot fully exclude the possibility that germline
252 DAF-16/FoxO plays a role in mediating DAF-2/IGFR's effects on GSPC mitotic timing, our results
253 are most consistent with the notion that DAF-16/FoxO, like DAF-2/IGFR, acts primarily in the
254 soma.

255 To further pinpoint the somatic tissues involved, we used the AID system to deplete DAF-
256 2::AID::mNG from neurons (*rgef-1p::TIR1*), muscle (*myo-3p::TIR1*), intestine (*ges-1p::TIR1*),
257 hypodermis (*dpy-7p::TIR1*) and gonadal somatic sheath cells (*lim-7p::TIR1*) (55). Depletion from
258 the intestine or gonadal sheath cells was sufficient to delay mitosis in GSPCs, while depletion
259 from other tissues had no effect (**Fig 3F**). Taken together, our data strongly suggests that the IIS
260 pathway, from DAF-2/IGFR to DAF-16/FoxO, acts in somatic tissues to maintain proper mitotic
261 timing in GSPCs, with the intestine and gonadal sheath cells being the principal foci of pathway
262 activity.

263

264 *Reduced IIS delays mitosis via the spindle assembly checkpoint but does not compromise mitotic*
265 *fidelity*

266 To determine how changes in IIS affect the duration of mitosis in GSPCs we first tested for
267 the involvement of the spindle assembly checkpoint. We used a null allele of the core checkpoint
268 gene *mdf-2*/Mad2 (*mdf-2(lt4)* (57); hereafter *mdf-2(0)*) to ablate checkpoint activity and assessed
269 GSPC mitotic duration in *mdf-2(0)* single and *daf-2(rf)*; *mdf-2(0)* double mutant animals. The

270 duration of mitosis in *mdf-2(0)* GSPCs was significantly reduced compared to control, consistent
271 with checkpoint regulation of basal mitotic timing in these cells (18), and GSPCs in *daf-2(rf)*; *mdf-*
272 *2(0)* double mutants had durations of mitosis that were indistinguishable from *mdf-2(0)* single
273 mutants (**Fig 4A**). Thus, *daf-2(rf)* mitotic delays are entirely dependent on an intact spindle
274 assembly checkpoint.

275 Checkpoint-dependent mitotic delays are typically due to defects in spindle assembly, and
276 correspondingly, accompanied by chromosome segregation errors when checkpoint surveillance
277 is removed. To determine whether reduced DAF-2/IGFR impairs spindle assembly, we asked
278 whether *daf-2(rf)*; *mdf-2(0)* GSPCs were more prone to mitotic errors. We used live-cell imaging
279 and scored GSPCs for mitotic errors using mCH::HIS-11 to monitor chromosome alignment and
280 segregation (**Fig 4B**). The frequency of mitotic errors in *daf-2(rf)* GSPCs was the same as control,
281 while *mdf-2(0)* GSPCs showed significantly more mitotic errors, as would be expected for
282 checkpoint-null cells (**Fig 4C**). Surprisingly, *daf-2(rf); mdf-2(0)* GSPCs showed the same frequency
283 of mitotic errors as *mdf-2(0)* cells (**Fig 4C**). We obtained similar results using putative null allele
284 of a second checkpoint gene *san-1*/Mad3 (*san-1(ok1580)* (44); hereafter *san-1(lf)*) (**S5A Fig**).
285 Correspondingly, several known checkpoint-null phenotypes that are associated with germline
286 function were not enhanced in *daf-2(rf); mdf-2(0)* animals, including embryonic lethality and
287 reduced brood size (58) (**Fig 4E-F**), nor did we observe increased germ cell apoptosis, which clears
288 nuclei with DNA damage and/or chromosome abnormalities (59-61) (**Fig 4G**). Altogether, we
289 conclude that reducing DAF-2/IGFR activity leads to checkpoint-dependent mitotic delays that
290 are not associated with defects in spindle assembly. Accordingly, in the absence of checkpoint
291 surveillance, reducing DAF-2/IGFR activity does not further compromise mitotic fidelity.

292 Interestingly, the one genetic interaction that we observed in *daf-2(rf); mdf-2(0)* animals was
293 enhanced sterility (**S5B Fig**). Both *daf-2(rf)* and *daf-2(rf); mdf-2(0)* germ lines had fewer mitotic
294 cells than controls, and *daf-2(rf); mdf-2(0)* germ lines tended to have fewer mitotic cells than *daf-*
295 *2(rf)* alone, although this difference was not statistically significant (9.4 +/-2.1, n=15 *daf-2(rf)*
296 versus 7.4 +/-2.8, n=15 *daf-2(rf); mdf-2(0)*; **S5C Fig**). Given the recently reported role for MDF-
297 2/Mad2 in promoting the G2/M transition independently of its involvement in the spindle
298 assembly checkpoint (57), and the known role of DAF-2/IGFR in promoting GSPC passage through
299 G2 (24), we speculate that enhanced sterility in *daf-2(rf), mdf-2(0)* animals may be due to
300 synergistic defects in GSPC cell cycle progression.
301
302 *Reduced IIS and caloric restriction delay mitosis via different pathways*
303 The effects of reduced IIS on GSPC mitosis are different from what we have previously
304 reported for caloric restriction. Caloric restriction leads to GSPC mitotic delays that depend on
305 the spindle assembly checkpoint, and a lower GSPC mitotic index (**S6A Fig**; (28)); however, caloric
306 restriction also enhances several phenotypes associated with increased chromosome
307 segregation errors when the checkpoint is impaired (18). We verified that caloric restriction
308 compromises mitotic fidelity by scoring the frequency of mitotic errors in animals fed a 1 in 10
309 dilution of their normal bacteria food source (sDR; (62)) with and without checkpoint regulation,
310 as done for *daf-2(rf)*. We found that sDR increased the frequency of mitotic errors in *san-1(lf)*
311 GSPCs, as compared to *san-1(lf)* GSPCs in animals fed *ad libitum* (**Fig 5A**). Thus, unlike the mitotic
312 delays caused by reduced IIS, mitotic delays upon caloric restriction reflect impaired spindle
313 assembly.

314 We next tested the genetic requirements for GSPC mitotic delays upon caloric restriction,
315 focusing on members of the IIS pathway. We used two methods to induce caloric restriction, a
316 mutation in *eat-2* (*eat-2(ad465)*; hereafter *eat-2(rf))* that slows pharyngeal pumping reducing
317 food intake (63), and sDR. For *eat-2(rf)* experiments, we used GFP::TBB-2 to visualize spindles
318 and measure mitotic timing. For sDR experiments, both spindles (GFP::TBB-2) and chromatin
319 (mCH::HIS-11) were marked, allowing us to measure both mitotic timing and mitotic index. We
320 found that *daf-16(lf)*, which fully suppressed mitotic delays in *daf-2(rf)* animals (**Fig 2B**), did not
321 suppress mitotic delays in either *eat-2(rf)* or sDR-treated animals (**Fig 5B-C**). The GSPC mitotic
322 index of sDR-treated *daf-16(lf)* animals also remained low (**S6B Fig**). These results indicate that
323 canonical DAF-2/IGFR to DAF-16/FoxO signaling does not mediate the effect of caloric restriction
324 on GSPC mitosis and, by extension, downstream effectors other than DAF-16/FoxO must be
325 involved.

326 *daf-18*/PTEN plays both *daf-16*/FoxO-dependent and independent roles in regulating GSPC
327 proliferation during development and adulthood (9-11, 24, 30, 35). We found that *daf-18(lf)*
328 restored normal mitotic timing in both *eat-2(rf)* and sDR-treated animals (**Fig 5B-C**) and rescued
329 the low mitotic index in sDR-treated animals (**S6B Fig**). In several situations where *daf-18*/PTEN
330 acts independently of *daf-16*/FoxO to regulate GSPC behavior, it acts upstream of, or in parallel
331 to, AMPK (31, 33). We tested for AMPK involvement using animals bearing null mutations in both
332 catalytic α subunits (*aak-1(tm1994)* and *aak-2(ok524)* (44, 64, 65); hereafter *aak-1/2(0)*). Like
333 *daf-18(lf)*, *aak-1/2(0)* also rescued GSPC mitotic delays and low mitotic index upon sDR (**Fig 5D**
334 **and S6C Fig**). Based on these results, we conclude that while caloric restriction and reduced IIS
335 both delay GSPC mitosis, they do so via distinct mechanisms.

336

337 **Discussion**

338 Here we have investigated the signaling requirements for proper GSPC mitotic timing as a
339 model for how stem and progenitor cell mitosis is regulated *in vivo*, in the whole-animal context.
340 Through our candidate screen we found that reducing the activity of *daf-2*/IGFR, *daf-7*/TGF-β or
341 *glp-1*/Notch prolongs the duration of mitosis in GSPCs. These results implicate three distinct
342 signaling pathways in the regulation of GSPC mitosis. Notably, of the three, only IIS plays a major
343 role in GSPC cell cycle progression (23-26, 66), suggesting that mitotic and cell cycle timing can
344 be uncoupled and may therefore be subject to distinct regulatory mechanisms. As only a subset
345 of the mutant backgrounds in our screen altered GSPC mitosis, we also infer that the effects we
346 have uncovered are unlikely to be a generic response to perturbed signaling compromising
347 animal health. This is further supported by our results showing that mitotic delays caused by
348 reduced IIS and caloric restriction can be suppressed genetically and rely on different
349 downstream signaling effectors. Together, these results argue that changes in the duration of
350 GSPC mitosis are not merely a nonspecific consequence of generally suboptimal conditions for
351 cell division, but rather the product of specific regulatory events.

352 Our data also suggest that delayed cells from different mutant backgrounds exhibit different
353 combinations of spindle features, which may indicate specificity in terms of the mitotic processes
354 that are affected. Further supporting this idea, we have shown that reduced IIS and caloric
355 restriction produce distinct phenotypes in terms of mitotic fidelity when the spindle assembly
356 checkpoint is impaired. Caloric restriction increases the frequency of chromosome segregation

357 errors, while reduced IIS does not, suggesting that the root cause of mitotic delays in each
358 condition are distinct.

359 We have previously proposed that caloric restriction delays GSPC mitosis by reducing the
360 availability of cellular energy, which impairs energy-dependent mitotic events like spindle
361 assembly and increases the amount of time it takes for cells to satisfy the checkpoint (18). Our
362 results showing that caloric restriction compromises accurate chromosome segregation when
363 checkpoint surveillance is removed are consistent with this idea. However, we have also shown
364 that mitotic delays upon caloric restriction require *daf-18*/PTEN and *aak-1/2*/AMPK, suggesting
365 that they are more precisely regulated than our earlier model might have anticipated. AMPK is a
366 highly conserved energy sensor that responds to low cellular energy by modifying both metabolic
367 and non-metabolic processes, including cell cycle progression (67). More recently, roles for AMPK
368 in mitosis have been uncovered in both mammalian cells and Drosophila (68-71). Our work
369 suggests that AMPK's involvement in mitosis is generally conserved and expands on previous
370 reports by showing that AMPK links mitosis to physiological changes such as dietary intake.

371 Unlike caloric restriction, reduced IIS does not appear to compromise spindle assembly. In
372 the absence of checkpoint regulation, these cells are no more likely to experience chromosome
373 segregation errors than cells in an unperturbed insulin signalling environment, ruling out defects
374 in kinetochore-microtubule attachment which would impede chromosome bi-orientation. This
375 then raises the question as to why they are delayed in mitosis? We have shown that these delays
376 are entirely dependent on the spindle assembly checkpoint, making it unlikely that they are due
377 to events following checkpoint satisfaction (e.g. a slower rate of APC/C-directed degradation of
378 cyclin B and/or Securin should slow mitotic progression with or without checkpoint activity (72)).

379 Instead, we think it more likely that reduced IIS affects the checkpoint itself, by enhancing
380 checkpoint activity and/or delaying checkpoint silencing. For example, reduced insulin signalling
381 could increase the strength of checkpoint signaling at individual kinetochores relative to their
382 attachment state (73, 74) or increase the microtubule occupancy threshold for checkpoint
383 silencing (75-79). Alternatively, the rate of MCC turnover in the cytoplasm could be slower (80-
384 86), favoring MCC accumulation and greater APC/C inhibition. Experiments to assess checkpoint
385 strength and kinetochore enrichment of checkpoint proteins in GSPCs when IIS is reduced will
386 help to differentiate between these possibilities and clarify the mechanism by which mitosis is
387 delayed. A role for IIS in modulating checkpoint strength would be particularly interesting as it
388 might serve to protect cells from environmental or physiological conditions that could
389 compromise mitotic fidelity and would therefore be adaptive.

390 In considering the nature of the changes to mitosis downstream of IIS, we also have to
391 account for the fact that the insulin pathway is acting cell non-autonomously. We found that both
392 DAF-2/IGFR and DAF-16/FoxO are present in GSPCs and that germline-specific depletion of DAF-
393 2/IGFR affects DAF-16/FoxO partitioning between the GSPC nucleus and cytoplasm, all of which
394 is consistent with germline autonomous DAF-2/IGFR to DAF-16/FoxO signal transduction.
395 However, neither DAF-2/IGFR nor DAF-16/FoxO are required in the germ line for normal GSPC
396 mitotic timing, while both are required in the soma. Based on these results, we conclude that IIS
397 in somatic tissues acts cell non-autonomously to impact mitosis in GSPCs.

398 This result was surprising given the prevailing model that larval GSPC proliferation is regulated
399 by germline-autonomous IIS (16, 24) and could suggest that anatomically distinct sites of IIS
400 activity affect GSPC cell cycle versus mitotic timing. In our experiments we did not have the

401 necessary markers to determine how tissue-specific DAF-2/IGFR depletion affected the GSPC
402 mitotic index, which is the standard metric for inferring cell cycle perturbations (16), and so could
403 not address this idea directly. However, the lower mitotic index in *daf-2(rf)* animals (**Figs 1E and**
404 **2B**) corresponded to fewer mitotic cells overall (8.2 +/-2.6, n=20 *daf-2(rf)* versus 14.7 +/-3.9, n=28
405 control; see also **S1B Fig**), and when we counted the total number of mitotic cells per germline
406 in our DAF-2::AID::mNG experiments, DAF-2 depletion from the soma or intestine phenocopied
407 *daf-2(rf)* with fewer mitotic cells (8.0 +/-2.9, n=10 soma and 8.1 +/-3.4, n=12 intestine), while
408 depletion from the germ line had no effect **(S4E-F Fig**). Thus, in our hands, the effects of reduced
409 IIS on GSPC mitosis and cell cycle progression appear to be coupled, with both being most
410 sensitive to DAF-2/IGFR activity in the soma, particularly in the intestine.

411 Cell non-autonomous IIS occurs when DAF-16/FoxO activity in one tissue influences IIS and
412 DAF-16/FoxO activity in a second tissue, so-called FoxO-to-FoxO signaling (87, 88), or when DAF-
413 16/FoxO-independent responses are induced in the signal receiving tissue (89, 90). As germline
414 DAF-16/FoxO was not necessary to delay GSPC mitosis we favor the latter mechanism. The lack
415 of a cell autonomous role for DAF-16/FoxO also rules out the possibility that DAF-16/FoxO-
416 dependent changes in GSPC gene expression determine GSPC mitotic timing. Thus, unlike
417 Forkhead family transcription factors in yeast and human cells, which affect the timing of mitotic
418 events and mitotic fidelity by regulating the expression of mitotic genes (5, 91, 92), DAF-16/FoxO
419 appears to influence mitotic timing in *C. elegans* GSPCs solely via its involvement in inter-organ
420 communication.

421 Based on our tissue-specific DAF-2/IGFR depletion experiments, the intestine and somatic
422 sheath cells are the likely sources for a DAF-16/FoxO-dependent secondary signal that acts on

423 GSPCs. In *C. elegans*, the intestine comprises the entire endoderm and serves as a major hub for
424 homeostatic regulation (93). Notably, intestinal IIS contributes to reproductive aging, including
425 age-related loss of GSPCs (27). The somatic sheath cells, which enwrap the germ line and are
426 connected to GSPCs by gap junctions for most of larval development, support GSPC proliferation
427 (41, 94-97) Thus both tissues are well positioned to regulate GSPC mitosis cell non-autonomously.
428 Determining the identity of the secondary signal which acts on GSPCs and how it interfaces with
429 mitosis will provide a framework for understanding how inter-organ communication contributes
430 to mitotic regulation.

431 **Materials and Methods**

432 *C. elegans strains and culture*

433 *C. elegans* strains were maintained at either 15°C or 20°C on nematode growth medium (NGM),
434 seeded with *Escherichia coli* (*E. coli*) strain OP50 (NGM/OP50), following standard protocols (98).
435 See **S1 Table** for the full list of strains used in this study. For live-cell imaging, animals were
436 synchronized at the L1 larval or embryonic stage and raised at 20°C, at a density of 30-40 larvae
437 per plate. Larvae were raised on standard NGM plates seeded with the *E. coli* strain HT115
438 (NGM/HT115), which produces more uniform developmental timing and a more consistently high
439 number of GSPC divisions (19, 99). Late L4 larvae were selected 2-4 days later, depending on
440 synchronization method and genetic background. For all experiments using thermosensitive
441 alleles (*daf-2(e1370)*, *glp-1(e2141)*, *glp-1(ar202)*, *mpk-1(ga111)*, *let-60(ga89)* and *daf-7(e1372)*),
442 animals were raised at the semi-permissive temperature of 20°C from the L1 stage. Synchronized
443 L1 larvae were obtained by sodium hypochlorite treatment (100) or by direct transfer from
444 recently starved NGM/OP50 plates. For sodium hypochlorite treatment, gravid adults were
445 washed from the surface of a standard NGM/OP50 plate using 1 ml M9 buffer (22 mM KH_2PO_4,
446 42 mM Na_2HPO_4, 86 mM NaCl, 1 mM $MgSO_4$), and dissolved in 1 ml of a solution of 1% NaClO
447 and 500 mM NaOH in water, for no more than 7 min, with regular agitation. Released embryos
448 were rinsed and incubated for 24hrs at 15°C in M9 with rotation. For direct transfer, strains were
449 maintained on NGM/OP50 plates by weekly transfer and small "clumps" of approximately L1
450 staged larvae were transferred by worm pick 1-3 days after the bacterial lawn had been fully
451 consumed. To obtain synchronized embryos, 3-5 adults were transferred to an NGM/HT115 plate
452 and let to lay eggs for 2-3 hrs, after which, adults were removed.

453

454 *Auxin treatment for AID depletion*

455 35 mm NGM plates containing 1 mM 1-naphthaleneacetic acid, potassium salt (K-NAA), a
456 synthetic auxin analog that is photostable and water soluble (101) (Phytotechnology Laboratories
457 N610) were seeded with 150 µl of HT115 and incubated at room temperature overnight. Control
458 plates with no K-NAA were prepared in parallel. For experiments using TIR1 expressed from the
459 *sun-1* (germ line), *rgef-1* (neurons), and *lim-7* (gonadal somatic sheath cells) promoters and DAF-
460 2::AID::mNG, plates were inoculated with L1 larvae and L4 larvae were selected 40-48 hr later for
461 live-cell imaging. In our hands, strains carrying TIR1 expressed from the *ges-1* (intestine), *myo-3*
462 (muscle), or *dpy-7* (hypodermis) promoters and DAF-2::AID::mNG entered dauer when raised
463 from the L1 stage on 1 mM K-NAA plates. To avoid dauer entry, L1 larvae were raised on control
464 plates for 24 hrs, after which they were transferred to 1 mM K-NAA or fresh control plates, and
465 late L4 larvae were selected for live-cell imaging 24 hrs later. L1 larvae carrying TIR1 expressed
466 from the *eft-3* (pan-soma) promoter and DAF-2::AID::mNG were dauer constitutive when raised
467 on 1 mM K-NAA plates. As animals raised on control (no K-NAA) plates showed a weak *daf-2*
468 phenotype, we did not further pursue auxin treatment of this strain. For experiments using DAF-
469 16::GFP::AID, animals were raised on 1 mM K-NAA or control plates from the L1 stage. We note
470 that weak depletion of AID-tagged proteins in animals raised on control plates (i.e. without
471 supplemental auxin) was evident in several of our experiments (*eft-3p::TIR1* with DAF-
472 2::AID::mNG, as noted above, and *sun-1p::TIR1* with DAF-2::AID::mNG, as seen by lower germline
473 fluorescence of DAF-2::AID::mNG (**Fig 3B**) and elevated nuclear DAF-16::GFP relative to other
474 controls (compare **Fig 2B** to **3B**)). Similar leaky degradation has been documented elsewhere

475 (102, 103). We also found that *eft-3p::TIR1*, which was designed to express TIR1 in the soma and
476 not in the germ line (54), lead to robust germline depletion of DAF-16::GFP::AID (**S4D Fig**),
477 suggesting that *eft-3p::TIR1* is at least weakly expressed in the germline and that this is sufficient
478 to drive degradation of some AID-tagged proteins.
479
480 *RNAi depletion of daf-2*
481 RNAi was performed by feeding, as described previously (104) with the following modifications.
482 A plasmid for the expression of double-stranded RNAi targeting *daf-2* was constructed by cloning
483 exon 9 of *daf-2* into the L4440 vector and transforming into the HT115 *E. coli* strain. Exon 9 of
484 *daf-2* was amplified with Phusion High-Fidelity DNA polymerase (New England Biolabs, M0530S)
485 using primers F_Primer: 5'-TAAGCACCATGGCACCTGTACCTTCTCCTTCAAC-3' and R_Primer: 5'-
486 TGCTTAGGGCCCCCTCTTCGATCGTCATGTTCTC-3'. The amplicon and L4440 vector were digested
487 using ApaI (New England Biolabs, R0114S) and NcoI (New England Biolabs, R0193S) restriction
488 enzymes. Ligation was performed using T4 DNA ligase (New England Biolabs, M0202S) and the
489 resulting plasmid was transformed into the HT115 *E. coli* strain following standard procedures.
490 HT115 carrying the *daf-2* plasmid or the empty vector L4440 were cultured for 12-16 hrs in LB +
491 100 µg/ml ampicillin (LB/Amp) at 37°C. This culture was diluted 1:100 in LB/Amp and grown for
492 another 6 hrs under the same conditions, after which 100 µl was added per 35 mm
493 NGM/IPTG/Carb plate (NGM with 1 mM isopropyl β-d-thiogalactoside (IPTG) and 50 µg/ml
494 carbenicillin). Seeded plates were kept in the dark, at room temperature for 3 days before adding
495 synchronized L1s. For experiments combining *daf-2(RNAi)* with AID depletion of DAF-16, plates

496 were prepared identically, except that 1 mM K-NAA was added to the NGM/IPTG/Carb plates at
497 the plate pouring stage.
498
499 *Dietary Restriction (sDR)*
500 35 mm plates containing standard NGM, with 50 µg/ml carbenicillin to prevent additional
501 bacterial growth, were seeded with 150 µl of HT115. A fresh overnight HT115 culture was used
502 either undiluted (control) or after a 1:10 dilution (sDR) in S basal (1M NaCl, 0.44M KH_2PO_4, 0.06M
503 K_2HPO_4, 0.05mg/mL Cholesterol). Plates were dried at room temperature for 24 hrs. Synchronous
504 cultures were obtained by egg collection, after rinsing adult animals in M9 buffer to reduce
505 bacterial transfer. Late L4 larvae were selected ~3 days later.
506
507 *Animal mounting and live-cell timelapse and single time point imaging*
508 Animals were mounted for live-cell imaging and/or single time point imaging as described in (19).
509 Briefly, animals were anesthetized in 0.04% tetramisole in M9 buffer and transferred to a 3%
510 agarose pad, molded using a silicon wafer etched to imprint square-shaped grooves 35 µm deep,
511 with widths ranging from 38-55 µm. Animals were positioned in grooves by gently blowing air
512 through a mouth pipet or using a worm eyelash pick. An 18 mm 1.5 coverslip was lowered gently,
513 the corners were sealed using VaLaP (1:1:1 Vaseline, lanolin, and paraffin) and the area under
514 the coverslip was backfilled with M9 + 0.04% tetramisole. For whole-animal imaging of DAF-
515 2::AID::mNG, animals were mounted following the same procedure except that 3% agarose pads
516 without grooves were used. Images were acquired at room temperature (~20°C) with either a
517 Quorum WaveFX-X1 spinning disk confocal (Leica DMI6000B inverted microscope, with an ASI

518 MS-2000 piezo stage, controlled by MetaMorph software, using a Leica 63x/1.40-0.60 HCX PL
519 APO oil immersion objective, 491 nm (50 mW) and 568 nm (50 mW) diode lasers, with ET 525/50
520 and FF 593/40 emission filters, using dual camera mode and two Photometrics PRIME BSI sCMOS
521 cameras), or a Nikon CSU-X1 spinning disk confocal (Nikon TI2-E inverted microscope with a
522 Yokogawa CSU-X1 confocal scanner, controlled by NIS-Elements software, using a Nikon Apo
523 40x/1.25 NA water immersion objective, 488 nm (100mW) and 561 nm (100mW) solid-state
524 lasers, with a dual band pass Chroma 59004m filter, and a Hamamatsu ORCA-Fusion BT sCMOS
525 camera). Specific imaging parameters are listed by experiment in **S2 Table.**
526
527 *Image processing and analysis*
528 All image processing and analysis was carried out in Fiji (105), using a combination of in-house,
529 semi-automated scripts and manual approaches, as specified below. Data were compiled and
530 analyzed in MATLAB (Mathworks), except where noted.
531
532 *Measuring mitotic duration and mitotic features using spindle pole tracking*
533 Spindle pole tracking and subsequent data analysis were performed as described in (18-20) with
534 minor modifications. In Fiji, images were converted from NIS-Elements or MetaMorph file
535 formats into a standard hyperstack TIF, with image metadata exported to a CSV file. Animal
536 movement was corrected prior to spindle pole tracking by XY registration, as described in (19,
537 20). Spindle pole tracking was performed using the TrackMate plug-in (106, 107). Tracks were
538 manually curated in TrackMate to create a relatively gap-free, single track per spindle pole, and
539 all spots in each track were renamed to indicate appropriate pairing (i.e. spindle poles belonging

540 to the same cell). The TrackMate 'Spots' information for each germ line was exported as a TXT
541 file and the XYZT coordinates and labels for all tracked spindle poles were imported into MATLAB
542 for scoring and analysis. Pole-to-pole distance (spindle length) was plotted relative to time and
543 NEBD, the "start" of mitosis, and anaphase onset were scored by clicking on spindle length versus
544 time plots, as previously described (18-20). If plots were ambiguous, cells were discarded or
545 scored visually using a cropped time-lapse. While NEBD is the definitive start of mitosis, we use
546 the first time point after NEBD at which spindle length reaches a stable minimum as the "start"
547 of mitosis for 2 reasons: (1) we find that NEBD is more difficult to unambiguously score from
548 spindle length plots; and (2) the time between NEBD and what we define as the "start" of mitosis
549 is relatively constant across strains and conditions and so not a major contributor to variation in
550 mitotic timing. These mitotic events were used as landmarks to calculate the duration of mitosis,
551 as described previously (19, 20), and mitotic features related to spindle size and dynamics.
552
553 *Analysis of GSPC mitotic features*
554 Mitotic features were calculated in MATLAB. The following features were extracted:
555 A. Pole separation prior to NEBD: the mean of the top 3 spindle length measurements within 3
556 min prior to NEBD.
557 B. Duration of mitosis: as described previously.
558 C. Spindle length: mean spindle length between the "start" of mitosis (t_S) and anaphase onset
559 (t_{AO})

560 D. Spindle length variance: the standard deviation for a random sampling of 7 spindle length
561 measurements between t_s and t_{AO}, after spindle length was normalized to mean spindle length
562 (as defined in C).
563 E. Spindle length fluctuation: the mean rate of change in spindle length, frame-to-frame,
564 throughout mitosis, calculated as the change in spindle length between frames, as a percent of
565 mean spindle length (as defined in C), divided by the frame rate.
566 F. Spindle rotation: the mean rate of spindle rotation, frame-to-frame, throughout mitosis,
567 calculated as the angle between spindle vectors in adjacent frames divided by the frame rate (i.e.
568 angular velocity).
569 G. Spindle elongation rate: the mean rate of change in spindle length between t_{AO} and 2.5 min
570 after t_{AO}, calculated as the slope of the line fit to spindle length versus time within this time
571 window.
572 H. Spindle rotation anaphase: as in F, but measured between t_{AO} and 2.5 min after t_{AO}.
573 I. Pole separation telophase: the second largest spindle length measured at least 7 min after t_{AO}
574 and expressed as a percent of mean spindle length (as defined in C).
575 Raw data are in **S1 Data**. Feature name abbreviations are preserved for compatibility with
576 MATLAB scripts. Letters correspond to descriptions given above.
577 To generate the heatmap in S2B Fig, outliers were removed for all features except duration of
578 mitosis. Outliers were defined as values that were more than 1.5x the interquartile range above
579 the 75th quartile or below the 25th quartile. Outliers for each feature were assessed on a per
580 genotype basis (e.g. outliers within the *daf-2(e1370)* data were defined based on the *daf-*
581 *2(e1370)* values). A Kruskal-Wallis test with a Tukey-Kramer post hoc test (MATLAB *kruskalwallis*

582 and *multcompare*) was performed, with a threshold for significance of $p < 0.05$, to determine
583 whether any genotype was statistically different from control (shown as asterisks in the
584 heatmap). The mean value for each feature for each genotype was normalized to control, and
585 these normalized values (# standard deviations above/below control mean) were plotted as a
586 heatmap (MATLAB *heatmap*). To determine whether any mitotic feature correlated with mitotic
587 duration across all genotypes (S2C Fig), all measurements for a given feature were combined,
588 standardized ($x - \mu/\sigma$), and tested for a correlative relationship with the duration of mitosis by
589 assessing the Pearson's linear correlation coefficient (r) and *p* value, after Bonferroni correction
590 for multiple testing. Features showing a correlation with $p < 0.05$ were plotted as a heatmap as
591 above. Non-significant correlations are shown as 0. Principal component analysis (S2D Fig) was
592 performed after data standardization using the *pca* function in MATLAB. Data were plotted along
593 the first two principal components, which account for ~45% of the total variance, and features
594 were overlaid using the *biplot* function. Cells were classified as "delayed" if their duration of
595 mitosis was greater than the 90th percentile of the control dataset published in (20). Delayed cells
596 from *daf-2(e1370)*, *daf-7(e1372)* and *glp-1(e2141)* are colored-coded accordingly.
597
598 *Measuring the number of mitotic GSPCs, the number of PZ nuclei and the PZ mitotic index*
599 The number of mitotic GSPCs, number of PZ nuclei and the PZ mitotic index were measured in
600 the same germ lines as were used for live-cell imaging. After XY registration, any germ lines in
601 which the distal germ line was cut off in XY or Z were excluded. Mitotic cells were counted at the
602 first frame, using the GFP or mCH::TBB-2 signal to identify all cells in which 2 spindle poles could
603 be easily discerned (i.e. all cells in early prophase through early telophase). Mitotic cells were

604 scored manually in Fiji using the point selection tool and saving the location of all scored cells as
605 an ROI list. For stains carrying HIS-11::mCH, the total number of cells in the PZ was counted as
606 the number of nuclei between the distal tip of the gonad and the first row of crescent shaped
607 meiotic nuclei (108, 109). Nuclei were counted from the first frame without appreciable animal
608 movement. PZ nuclei counts were obtained by re-purposing the spot detection tools available in
609 TrackMate (106, 107). After pre-processing the HIS-11::mCH channel (background subtraction,
610 median 3D filtering with X and Y radii = 2 µm and Z radius = 1 µm, and gaussian blurring with
611 sigma = 2) and manually defining a rectangular ROI encompassing the PZ, the Differences of the
612 Gaussian (DoG) blob detector (estimated blob diameter = 4.25 µm) and the linear assignment
613 problem (LAP) spot linker (maximum link and gap-closing distances = 3.0 µm, maximum gap
614 allowance = 2 frames), were used to identify and track nuclei over at least 5 frames. Spots were
615 manually curated to exclude non-nuclei spots (e.g. auto-fluorescent gut granules) or non-PZ
616 nuclei (e.g. nuclei in the proximal gonad arm). The TrackMate 'Spots' information for each PZ was
617 exported as a CSV file and the XYZ coordinates for all nuclei were imported into MATLAB to
618 extract nuclei counts, align nuclei counts with the respective number of mitotic cells and to
619 calculate the mitotic index (number of mitotic cells/number of PZ nuclei). We note that our PZ
620 nuclei counts for control strains are similar to reported values (41), while our mitotic indices are
621 higher (24), likely owing to the fact that we can detect cells across more mitotic stages (prophase
622 to telophase) than methods that count mitotic figures or phospho-Histone H3 positive cells.
623
624 *Measuring DAF-16::GFP nuclear enrichment*

625 For single time point images, 9 interphase nuclei per germ line were selected manually using the
626 HIS-11::mCH channel. A circular ROI, 4.5 µm in diameter, centered in XY and Z on each nucleus
627 was drawn manually using the oval area selection tool. To generate cytoplasmic ROIs, the radius
628 of each nuclear ROI was enlarged by 1 µm, and a donut-shaped composite ROI was generated
629 using the XOR function in the ROI manager. Neighboring nuclei were outlined manually using the
630 oval area selection tool and excluded from the cytoplasmic ROI using the XOR function (see **Fig**
631 **2D**). DAF-16::GFP fluorescence intensity (FI) was measured by applying these ROIs to the GFP
632 channel and measuring the mean FI per pixel within each. After background subtraction (the
633 mean FI per pixel across 3 rectangular ROIs positioned outside of the animal), the nuclear-to-
634 cytoplasmic ratio for each cell was calculated as the mean nuclear FI divided by the mean
635 cytoplasmic FI. To measure DAF-16::GFP nuclear enrichment in timelapse images, animal
636 movement was corrected by XY registration, as for spindle pole tracking. Mitotic nuclei were
637 tracked manually by drawing a 4.5 µm diameter circular ROI, centered in XY and Z on each
638 nucleus, over time. Cytoplasmic ROIs were generated and the DAF-16::GFP nuclear-to-
639 cytoplasmic ratio was calculated for each time point as described above. The coordinates of the
640 nuclear ROI were also used to generate an average intensity projection of 5 z-slices (0.75 µm step
641 size), centered in Z on the tracked nucleus over time. Changes in the variance of the HIS-11::mCH
642 FI within the nuclear ROI in these projections was used to estimate the duration of mitosis, as
643 described previously (18). Briefly, the HIS-11::mCH variance for each nucleus was min-max
644 normalized, and plotted relative to time in MATLAB. NEBD was scored as the last time point when
645 normalized variance was less than 50% of max and/or just prior to the sharp increase that
646 characterizes the start of chromosome congression. Anaphase onset was scored as the last time

647 point when normalized variance was greater than 70% of max and/or just prior to the sharp
648 decrease that characterizes the start of chromosome segregation. Plots were scored using *ginput*
649 in MATLAB. The time of NEBD was used to extract the DAF-16::GFP nuclear-to-cytoplasmic ratio
650 prior to mitosis, by taking the mean of the highest 3 values measured at least 10 min prior to
651 NEBD. 10 min was selected as the nuclear-to-cytoplasmic ratios measured at this time were
652 similar to interphase nuclei. After 10 min, nuclear DAF-16::GFP decreases (See **Fig 2E**).
653
654 *Measuring DAF-2::AID::mNG and DAF-16::GFP::AID germ line depletion*
655 2-channel, single time point Z-stacks were taken prior to the start of live-cell imaging for a subset
656 of the germ lines used for spindle pole tracking in Fig 3E. The middle z-slice for each germ line
657 was selected using TBB-2::mCH signal. For DAF-2::AID::mNG measurements, a maximum
658 intensity projection of 7 z-slices (0.75 µm step size), centered at this mid-plane, was generated.
659 For DAF-16::GFP::AID measurements, the mid-plane z-slice was used. Three rectangular ROIs
660 (~9.7 x 12.9 µm) were drawn within the distal germ line region using the TBB-2::mCH signal and
661 used to measure the mean FI. Background FI was measured by performing the same procedure
662 for strains carrying *sun-1p::TIR1* or *eft-3p::TIR1* and TBB-2::mCH alone. Germ lines with FI less
663 than or equal to background were set to 0 and data were normalized to the relevant *sun-1p::TIR1*
664 no Auxin condition.
665
666 *Scoring mitotic errors in GSCs*
667 Mitotic cells were tracked using either the TBB-2::GFP signal and spindle pole tracking, as
668 described above, or the HIS-11::mCH signal, as described for counting PZ nuclei, followed by

669 manual curation in TrackMate (106, 107) to label mitotic nuclei. Tracking coordinates were used
670 to generate a cropped maximum intensity projection (11 z-slices, 0.5 µm step size) of each cell.
671 Cropped cells were collected in a single folder and file names were replaced with an arbitrary
672 number such that users were blind to the genotype of each cell during scoring. Cells were scored
673 manually using a semi-automated script that opened each file and allowed users to score cells
674 according to the following criteria: (1) no obvious defects; (2) misaligned chromosomes during
675 prometaphase/metaphase; (3) lagging, bridging and/or misaligned chromosomes during
676 anaphase.
677
678 *Measuring progeny production*
679 L4 stage larvae from well fed NGM/OP50 plates were singled onto new NGM/OP50 plates and
680 incubated at 20°C. Animals were transferred to new plates every 24 hrs for a total of 72 hrs. The
681 total number of mature adults on each plate 72 hrs later was counted manually using a
682 stereomicroscope. Animals that were sterile, dead, or bagged, were excluded from the analysis.
683 Data were compiled in Excel.
684
685 *Measuring embryonic lethality*
686 L4 stage larvae from well fed NGM/OP50 plates were transferred to a new NGM/OP50 plate and
687 left to develop to adulthood for 24 hrs at 20°C. Synchronous 1-day adults were then singled onto
688 new NGM/OP50 plates and allowed to lay eggs for 8hr at 20°C. Using a stereomicroscope, the
689 total number of eggs laid were counted at the end of the 8hr collection. 24 hrs later the number

690 of unhatched eggs were counted. Percent embryonic lethality was calculated as the number of
691 unhatched eggs divided by the total number of eggs laid. Data were compiled in Excel.
692
693 *Measuring sterility*
694 100 L4 stage larvae were transferred from well fed NGM + OP50 plates to new NGM + OP50
695 plates, 5 larvae per plate, and left to develop for 48 hrs at 20°C. Adults were scored manually,
696 using a stereomicroscope, as fertile, defined by a clear row of embryos *in utero,* or as sterile,
697 defined by an absence of embryos *in utero* and signs of abnormal germ line morphology (e.g.
698 highly reduced germ lines). Animals that were dead were excluded from the analysis. Animals
699 that bagged were counted as fertile. Data were compiled in Excel.
700
701 *Counting germ line apoptotic bodies*
702 L4 stage larvae expressing a CED-1::GFP fusion protein in the somatic sheath cells were
703 transferred from well fed NGM/OP50 plates to fresh plates and allowed to develop for 24 hr at
704 20°C to reach the adult stage. 1-day adults were mounted as for live-cell imaging and single time-
705 point z-stack images of the gonadal loop region were captured. Cell corpses were identified using
706 the CED-1::GFP signal, which accumulates between dying cells and those that are engulfing them
707 (110). Gonads were scored manually, with genotype information removed (as for mitotic error
708 scoring) to minimize user bias.
709
710 *Statistics and figure assembly*

711 Statistical analyses and data plotting were performed in MATLAB. Summary statistics for all
712 experiments, including statistical tests used, are provided in **S2 Data**. Figures were assembled
713 using Adobe Illustrator. For all plots showing GSPC mitotic duration, small dots represent
714 individual GSPCs, larger dots represent the mean duration of mitosis per gonad arm/PZ. For all
715 other plots, dots represent one gonad arm/PZ and/or one animal. For all experiments, one gonad
716 arm was assessed per animal. Boxplots show the median, interquartile range and most extreme
717 values not considered outliers. Bar plots show the mean with error bars showing the standard
718 deviation. n.s. = $p > 0.05$, * = $p < 0.05$, ** = $p < 0.01$, *** = $p < 0.001$. All representative images
719 were scaled to the same brightness and contrast settings, pseudo colored and cropped in Fiji,
720 before exporting as RGB TIFs. Rotated images are indicated by the inclusion of background-
721 colored pixels. Images were re-sized and/or masked in Adobe Illustrator to fit the final figure
722 panel.
723

724 **Acknowledgements**

725 We thank Drs. R. Roy (McGill), C. Rocheleau (McGill), S. Weber (McGill) and J.-C. Labbé (IRIC,
726 UdeM), members of the Gerhold and Weber labs, and members of the Montreal Area Worm
727 Meeting group for helpful feedback and sharing protocols, reagents and strains. We are also
728 grateful to Drs. P. Lara-Gonzalez (UC Irvine), A. Desai (UCSD) and B. Lacroix (CRBM) for sharing
729 strains. Some strains were provided by the CGC, which is funded by NIH Office of Research
730 Infrastructure Programs (P40 OD010440). We thank Wormbase (111), which was used regularly
731 throughout this project, and our funding sources.
732

733 **Supporting Information**

734 **S1 Fig**. Related to Fig 1. Number of nuclei per PZ (A) and number of mitotic cells per PZ (B) used
735 to calculate the mitotic index, as shown in Fig 1C and E. The dashed grey line indicates the median
736 value for control.

737

738 **S2 Fig**. Related to Fig 1. (A) Schematic showing the mitotic features extracted for GSPCs from
739 animals bearing mutant alleles in the signaling pathways shown in Fig 1B. Features are shown
740 relative to the spindle length versus time plot from Fig 1D, indicating which stage of mitosis they
741 relate to. Features are listed on the right with letter designations used in (B-D). (B) Heatmap
742 showing the mitotic features that differ significantly from control in each mutant background.
743 Data were compared using a Kruskal-Wallis with Tukey-Kramer post hoc test with the null
744 hypothesis that all samples come from the same distribution. Red indicates values above the
745 control mean and blue indicates values below the control mean. Color saturation indicates the
746 distance above/below the control mean after data standardization. (C) Heatmap showing the
747 strength of the linear relationship between each mitotic feature and the duration of mitosis
748 across all cells of all genotypes. Pearson's coefficient (r) is shown for significant ($p < 0.05$ after
749 Bonferroni correction) correlations. (D) Principal component analysis of mitotic features showing
750 all cells plotted along the first two principal components, with delayed cells (duration of mitosis
751 > 90th percentile of control) shown for *daf-2(e1370)*, *daf-7(e1372)* and *glp-1(e2141)*. Vectors
752 represent the contribution of each mitotic feature to the principal components shown.

753

754 **S3 Fig.** Related to Fig 2. (A) The PZ mitotic index in animals bearing the mutant alleles or allele
755 combinations indicated. *daf-18(nr2037)*, *akt-1(mg144)* and *daf-16(mu86)* rescue the lower
756 mitotic index seen in *daf-2(e1370)* animals. (B) The DAF-16::GFP nuclear-to-cytoplasmic ratio
757 (N:C) is elevated in GSPCs from animals in which *daf-2* was knocked down by RNAi. (C) Single time
758 point maximum intensity projections showing DAF-16::GFP nuclear localization over the course
759 of a GSPC mitosis. Numbers indicate time in minutes relative to mitosis start, as inferred from
760 HIS-11::mCH variance. Scale bar = 5 µm.
761
762 **S4 Fig.** Related to Fig 3. (A) Maximum intensity projection of the distal germ line of a late L4 larvae
763 showing DAF-2::AID::mNG (green) and germ cell membranes (magenta; tagRFP::PH). DAF-
764 2::AID::mNG is shown in inverted grey scale below. DAF-2::AID::mNG in the distal germ line is
765 predominantly found in cytoplasmic puncta (arrow heads) in GSPCs and in the rachis (the shared
766 inner core of cytoplasm to which all germ cells are connected via cytoplasmic bridges). Scale bar
767 = 10µm. (B) GSPC mitosis is delayed in animals after *daf-2* was depleted by RNAi throughout the
768 whole worm but not when *daf-2* was depleted in the germ line alone. (C) Lower magnification,
769 whole worm images showing partial DAF-2::AID::mNG depletion in *eft-3p::TIR1* animals without
770 auxin treatment. Orange arrow heads indicate prominent sites of somatic DAF-2::AID::mNG
771 expression (head neurons, vulva, intestine) in control animals (no TIR1; left) and the same
772 anatomical locations in animals bearing *eft-3p::TIR1* showing reduced expression. Scale bar =
773 50µm. (D) Single z-slice sections through the middle of the germ line (orange outline; left), or a
774 basal region through intestinal nuclei (blue arrow heads; right) in the same animals, showing DAF-
775 16::GFP::AID expression in *daf-2*(RNAi) treated animals. As with DAF-2::AID::mNG, *eft-3p::TIR1*

776 leads to partial somatic depletion of DAF-16::GFP::AID without the addition of auxin (compare
777 top intestinal nuclei to those in either of the bottom 2 images). Auxin treatment leads to nearly
778 complete DAF-16::GFP::AID depletion, in both germ line and soma, in *eft-3p::TIR1* animals, and
779 robust germ line depletion in *sun-1p::TIR1* animals. Scale bar = 20µm. Quantification of germ line
780 DAF-16::GFP::AID fluorescence for a subset of the animals assayed in Fig 3E is shown on the right.
781 (E) and (F) The number of mitotic cells per PZ for a subset of the germ lines assessed in Figs 3D
782 and 3F. Fewer mitotic cells were seen in the PZs of *eft-3p::TIR1* animals, although this difference
783 was not statistically significant, and in the PZs of *ges-1p::TIR1* animals after auxin treatment. Dots
784 represent individual PZs.
785
786 **S5 Fig.** Related to Fig 4. (A) The percent of cells showing mitotic errors, as shown in Fig 4C, for
787 *san-1(ok1580)* single mutants and *daf-2(e1370); san-1(ok1580)* double mutants. The total
788 number of cells scored for each genotype is shown at the base of each stacked bar plot. *daf-*
789 *2(e1370)* does not increase the frequency of mitotic errors in *san-1(ok1580)* mutants. (B) The
790 percent of L4 larvae that develop into sterile versus fertile/gravid adults. The total number of
791 animals scored for each genotype is shown at the base of each stacked bar plot. *daf-2(e1370)*
792 enhances the sterility of *mdf-2(lt4)* mutants. (C) The number of mitotic cells per PZ for a subset
793 of the germ lines assessed in Fig 4A. The number of mitotic cells is slightly lower in *daf-2(e1370);*
794 *mdf-2(lt4)* double mutants than in daf-2(e1370) alone, although this difference is not statistically
795 significant.
796

797 **S6 Fig.** Related to Fig 5. The mitotic index for animals fed *ad libitum* (adL) versus those subjected
798 to caloric restriction (sDR) for control (A), *daf-16(mu86)* and *daf-18(nr2037)* mutants (B) and
799 AMPK null animals (*aak-1(tm1944); aak-2(ok425)*) (C). The mitotic index was measured for a
800 subset of the animals assayed in Fig 5C and D. Similarly to mitotic duration, the low mitotic index
801 in sDR animals requires *daf-18* and *aak-1/2*, but not *daf-16*.
802
803 **S1 Table.** Strain list. Unless otherwise indicated, all strains were generated as part of this study,
804 by standard genetic crosses. The source strains for alleles and transgenes are indicated the first
805 time a strain carrying them appears in the table.
806
807 **S2 Table.** Imaging parameters. Imaging parameters are listed by experiment type with relevant
808 figures indicated. Imaging parameters were held constant across experiments with occasional
809 exceptions. Where multiple settings were used, the most common are in bold. For spindle pole
810 and mitotic error tracking, variation in imaging parameters was within the range commonly used
811 by our lab and below the threshold for phototoxicity as determined in (20). For experiments
812 quantifying fluorescence intensity, data were normalized to the same point of reference to
813 permit comparison across experiments.
814
815 **S1 Data**. Candidate screen mitotic features
816
817 **S2 Data**. Summary statistics for all figures

818 **Figure Legends**

819 **Fig 1**. Mutations in *daf-2*/IGFR, *daf-7*/TGF-β and *glp-1*/Notch delay GSPC mitosis. (A) Cartoon
820 representation showing the organization of the *C. elegans* somatic gonad and germ line in adults
821 (top) and L4 larvae (bottom), with a close up of the distal proliferative zone (PZ), which houses
822 GSPCs. (B) Schematic illustrating the role of conserved signaling pathways in regulating GSPC fate
823 and/or cell cycle progression and whether they act in the soma or germ line. Major points of
824 regulation are indicated by line weight. (C) A maximum intensity projection through the top
825 portion of the distal region of one gonad arm from an L4 larva expressing GFP::TBB-2 (top) and
826 HIS-11::mCH (bottom) in germ cells. Arrow heads (top) show examples of mitotic spindles in
827 different stages of mitosis (prophase through telophase). The PZ is outlined (bottom), with an
828 arrow indicating a crescent-shaped meiotic nucleus marking the proximal end of the PZ. The
829 mitotic index is calculated by dividing the total number of cells with 2 centrosomes by the number
830 of nuclei in the PZ. Scale bar = 10 µm. (D) Single time point, maximum intensity projections of
831 GFP::TBB-2 (top) and HIS-11::mCH (bottom) during GSPC mitosis, with a plot of spindle length
832 over time for the cell shown. Numbers indicate time in minutes, relative to the metaphase-
833 anaphase transition, for different mitotic phases or key transitions. Pro = Prophase, NEBD =
834 nuclear envelope breakdown, start = first time point after NEBD when spindle length stabilizes,
835 end = metaphase-anaphase transition, Ana = Anaphase, Telo = Telophase. Scale bar = 5 µm. (E-F)
836 The PZ mitotic index (E) and GSPC duration of mitosis (F) in L4 larvae bearing mutant alleles in
837 the signaling pathways shown in B. The dashed grey line indicates the median value for control.
838 The mitotic index is lower in *daf-2(e1370)* animals and mitosis is delayed in *daf-2(e1370)*, *glp-*
839 *1(e2141)* and *daf-7(e1372)* animals.

840

841 **Fig 2**. *daf-2(e1370)* delays GSPC mitosis via the canonical IIS pathway converging on DAF-
842 16/FoxO. (A) Schematic showing the core IIS pathway with pathway components color-coded as
843 in (B). (B) The duration of GSPC mitosis in animals bearing the mutant alleles or allele
844 combinations indicated. *daf-2(e1370)* mitotic delays are suppressed by loss-of-function
845 mutations in *daf-18* and *daf-16* and a gain-of-function mutation in *akt-1*. The dashed grey line
846 indicates the median value for control. *daf-2(e1370)* is delayed relative to all other genotypes.
847 All other genotypes are similar to control. (C) Maximum intensity projections of the top half of a
848 gonad arm from control (top) and *daf-2(e1370)* (bottom) L4 larvae expressing DAF-16::GFP, from
849 the endogenous *daf-16* locus, and HIS-11::mCH in germ cells. Yellow boxes indicate the cells
850 shown in (D). (D) Maximum intensity projections of single control (top) and *daf-2(e1370)*
851 (bottom) GSPC nuclei. Blue and yellow overlays show the regions used to measure DAF-16::GFP
852 cytoplasmic and nuclear fluorescence intensity, respectively. (E) The DAF-16::GFP nuclear-to-
853 cytoplasmic ratio (N:C) is elevated in *daf-2(e1370)* GSPCs relative to control. (F) Changes in the
854 DAF-16::GFP N:C (green) and HIS-11::mCH variance (magenta) over time relative to mitosis start
855 for *daf-2(e1370)* GSPCs. Grey shaded region shows the period of time prior to the start of mitosis
856 when DAF-16::GFP was measured for mitotic cells. Mitotic duration was inferred from changes
857 in the variance of HIS-11::mCH. (G) DAF-16::GFP N:C prior to mitosis does not predict the duration
858 of mitosis on a per cell (x) basis. Grey line shows the linear least-squares best fit for the data, with
859 Pearson's coefficient and *p* value shown below.

860

861 **Fig 3**. The IIS pathway acts cell non-autonomously from the soma to regulate GSPC mitosis. (A)
862 Maximum intensity projections showing DAF-2::AID::mNG in the germline (outlined in orange)
863 and developing vulva (blue arrow head) in animals carrying *sun-1p*::*TIR1* with (middle) and
864 without (top) auxin treatment, and *eft-3p*::*TIR1* (bottom) without auxin treatment. The vulva is
865 shown as an example of somatic depletion in *eft-3*::*TIR1,* but not in *sun-1p::TIR1,* animals. Scale
866 bar = 10µm. (B-D) The mean DAF-2::AID::mNG fluorescence intensity per distal germ line,
867 normalized to *sun-1p*::*TIR1* no auxin (B), the GSPC DAF-16::GFP nuclear-to-cytoplasmic ratio (N:C)
868 (C), and the duration of GSPC mitosis (D) in *sun-1p::TIR1* animals with and without auxin, and *eft-*
869 *3p::TIR1* animals without auxin. Auxin treatment of *sun-1p::TIR1* animals depletes DAF-
870 2::AID::mNG in the germ line, increases the GSPC DAF-16::GFP N:C, but does not delay GSPC
871 mitosis. DAF-2::AID::mNG germline expression and the GSPC DAF-16::GFP N:C in *eft-3p::TIR1* no
872 auxin are similar to *sun-1p::TIR1* no auxin, yet GSPC mitosis is delayed. (E) The duration of GSPC
873 mitosis in animals after *daf-2* was depleted by RNAi (purple) compared to control (grey), with and
874 without auxin treatment to deplete DAF-16::GFP::AID in the germ line (*sun-1p::TIR1*) or in all
875 tissues (*eft-3p::TIR1*). DAF-16/FoxO depletion in the germ line does not suppress GSPC mitotic
876 delays induced by *daf-2*(RNAi), while *eft-3p::TIR1*-driven depletion of DAF-16, which affects both
877 soma and germ line (**S4 Fig**), does. (F) The duration of GSPC mitosis in animals after DAF-
878 2::AID::mNG was depleted in different somatic tissues. Depletion in the somatic gonadal sheath
879 cells (*lim-7p*) or intestine (*ges-1p*) was sufficient to delay GSPC mitosis.
880
881 **Fig 4.** Reduced IIS leads to checkpoint-dependent mitotic delays without compromising mitotic
882 fidelity. (A) The duration of GSPC mitosis in *daf-2(e1370)* and *mdf-2(lt4)* single mutants and *daf-*

883 *2(e1370); mdf-2(lt4)* double mutants compared to control. Loss of the checkpoint, via *mdf-2(lt4)*,
884 suppresses *daf-2(e1370)* mitotic delays entirely. (B) Single time point, maximum intensity
885 projections of GFP::TBB-2 (green) and HIS-11::mCH (magenta) during GSPC mitosis, with the HIS-
886 11::mCH channel shown in inverted grey scale below. Numbers indicate time in minutes, relative
887 to the metaphase-anaphase transition. Orange arrowhead indicates a chromosome that fails to
888 align at the metaphase plate and segregates improperly in anaphase. Scale bar = 5 µm. (C) The
889 percent of cells showing mitotic errors, as shown in (C), for *daf-2(e1370)* and *mdf-2(lt4)* single
890 mutants and *daf-2(e1370); mdf-2(lt4)* double mutants as compared to control. The total number
891 of cells scored for each genotype is shown at the base of each stacked bar plot. *daf-2(e1370)* does
892 not increase the frequency of mitotic errors in *mdf-2(lt4)* mutants. (D) Percent embryonic
893 lethality (dead embryos/total embryos laid) as assessed for individual animals. Animals were
894 binned according to the percent embryonic lethality shown on the right. The number of animals
895 scored per genotype is shown at the base of each stacked bar plot. (E) The total number of
896 progeny produced over a 3 day period for individual animals. (F) The number of apoptotic bodies
897 per gonad arm. *daf-2(e1370)* does not increase the severity *mdf-2(lt4)* embryonic lethality, low
898 brood size and elevated germline apoptosis.
899
900 **Fig 5.** Reduced IIS and caloric restriction rely on different downstream signaling effectors to delay
901 GSPC mitosis. (A) The percent of cells showing mitotic errors for animals fed *ad libitum* (adL) or
902 subjected to caloric restriction (sDR) in control versus *san-1(ok1580)* single mutants. The total
903 number of cells scored for each condition is shown at the base of each stacked bar plot. Unlike
904 *daf-2(e1370)*, sDR increases the frequency of mitotic errors in *san-1(ok1580)* mutants. (B-D) The

905 duration of GSPC mitosis in *eat-2(ad465)* single mutants compared to control, *daf-16(mu86)*; *eat-*
906 *2(ad465)* and *eat-2(ad465); daf-18(nr2037)* double mutants (B), in control versus *daf-16(mu86)*
907 and *daf-18(nr2037)* single mutant adL and sDR animals (C) and in AMPK null animals (*aak-*
908 *1(tm1944); aak-2(ok425)*) fed *ad libitum* or subjected to sDR (D). GSPC mitotic delays upon caloric
909 restriction depend on *daf-18* and *aak-1/2*, but not *daf-16*.

910 **References**

911 1. Duronio RJ, Xiong Y. Signaling pathways that control cell proliferation. Cold Spring Harb
912 Perspect Biol. 2013;5(3):a008904.
913 2. Lara-Gonzalez P, Pines J, Desai A. Spindle assembly checkpoint activation and silencing
914 at kinetochores. Semin Cell Dev Biol. 2021;117:86-98.
915 3. Levine MS, Holland AJ. The impact of mitotic errors on cell proliferation and
916 tumorigenesis. Genes Dev. 2018;32(9-10):620-38.
917 4. Herman JA, Romain RR, Hoellerbauer P, Shirnekhi HK, King DC, DeLuca KF, et al. Hyper-
918 active RAS/MAPK introduces cancer-specific mitotic vulnerabilities. Proc Natl Acad Sci U S A.
919 2022;119(41):e2208255119.
920 5. Alvarez B, Martinez AC, Burgering BM, Carrera AC. Forkhead transcription factors
921 contribute to execution of the mitotic programme in mammals. Nature. 2001;413(6857):744-7.
922 6. Gupta A, Yang Q, Pandita RK, Hunt CR, Xiang T, Misri S, et al. Cell cycle checkpoint
923 defects contribute to genomic instability in PTEN deficient cells independent of DNA DSB repair.
924 Cell Cycle. 2009;8(14):2198-210.
925 7. Manohar S, Yu Q, Gygi SP, King RW. The Insulin Receptor Adaptor IRS2 is an APC/C
926 Substrate That Promotes Cell Cycle Protein Expression and a Robust Spindle Assembly
927 Checkpoint. Mol Cell Proteomics. 2020;19(9):1450-67.
928 8. Shirakawa J, Fernandez M, Takatani T, El Ouaamari A, Jungtrakoon P, Okawa ER, et al.
929 Insulin Signaling Regulates the FoxM1/PLK1/CENP-A Pathway to Promote Adaptive Pancreatic
930 β Cell Proliferation. Cell Metab. 2017;25(4):868-82.e5.
931 9. Fukuyama M, Rougvie AE, Rothman JH. C. elegans DAF-18/PTEN mediates nutrient-
932 dependent arrest of cell cycle and growth in the germline. Curr Biol. 2006;16(8):773-9.
933 10. Narbonne P, Roy R. Inhibition of germline proliferation during C. elegans dauer
934 development requires PTEN, LKB1 and AMPK signalling. Development. 2006;133(4):611-9.
935 11. Narbonne P, Maddox PS, Labbé J-C. DAF-18/PTEN locally antagonizes insulin signalling to
936 couple germline stem cell proliferation to oocyte needs in C. elegans. Development.
937 2015;142(24):4230-41.
938 12. Angelo G, Van Gilst MR. Starvation protects germline stem cells and extends
939 reproductive longevity in C. elegans. Science. 2009;326(5955):954-8.
940 13. Kocsisova Z, Kornfeld K, Schedl T. Rapid population-wide declines in stem cell number
941 and activity during reproductive aging in C. elegans. Development. 2019;146(8).
942 14. Seidel HS, Kimble J. Cell-cycle quiescence maintains Caenorhabditis elegans germline
943 stem cells independent of GLP-1/Notch. Elife. 2015;4.
944 15. Korta DZ, Hubbard EJ. Soma-germline interactions that influence germline proliferation
945 in Caenorhabditis elegans. Dev Dyn. 2010;239(5):1449-59.
946 16. Hubbard EJA, Schedl T. Biology of the Caenorhabditis elegans Germline Stem Cell
947 System. Genetics. 2019;213(4):1145-88.
948 17. Morrison SJ, Kimble J. Asymmetric and symmetric stem-cell divisions in development
949 and cancer. Nature. 2006;441(7097):1068-74.
950 18. Gerhold AR, Ryan J, Vallée-Trudeau JN, Dorn JF, Labbé JC, Maddox PS. Investigating the
951 regulation of stem and progenitor cell mitotic progression by in situ imaging. Curr Biol.
952 2015;25(9):1123-34.

953 19. Zellag RM, Zhao Y, Gerhold AR. Live-cell Imaging and Analysis of Germline Stem Cell
954 Mitosis in Caenorhabditis elegans. Bio Protoc. 2022;12(1):e4272.
955 20. Zellag RM, Zhao Y, Poupart V, Singh R, Labbé JC, Gerhold AR. CentTracker: a trainable,
956 machine-learning-based tool for large-scale analyses of Caenorhabditis elegans germline stem
957 cell mitosis. Mol Biol Cell. 2021;32(9):915-30.
958 21. Hubbard EJ, Korta DZ, Dalfó D. Physiological control of germline development. Adv Exp
959 Med Biol. 2013;757:101-31.
960 22. Austin J, Kimble J. glp-1 is required in the germ line for regulation of the decision
961 between mitosis and meiosis in C. elegans. Cell. 1987;51(4):589-99.
962 23. Fox PM, Schedl T. Analysis of Germline Stem Cell Differentiation Following Loss of GLP-1
963 Notch Activity in Caenorhabditis elegans. Genetics. 2015;201(1):167-84.
964 24. Michaelson D, Korta DZ, Capua Y, Hubbard EJ. Insulin signaling promotes germline
965 proliferation in C. elegans. Development. 2010;137(4):671-80.
966 25. Dalfo D, Michaelson D, Hubbard EJ. Sensory regulation of the C. elegans germline
967 through TGF-beta-dependent signaling in the niche. Curr Biol. 2012;22(8):712-9.
968 26. Pekar O, Ow MC, Hui KY, Noyes MB, Hall SE, Hubbard EJA. Linking the environment,
969 DAF-7/TGFβ signaling and LAG-2/DSL ligand expression in the germline stem cell niche.
970 Development. 2017;144(16):2896-906.
971 27. Luo S, Kleemann GA, Ashraf JM, Shaw WM, Murphy CT. TGF-β and Insulin Signaling
972 Regulate Reproductive Aging via Oocyte and Germline Quality Maintenance. Cell.
973 2010;143(2):299-312.
974 28. Korta DZ, Tuck S, Hubbard EJ. S6K links cell fate, cell cycle and nutrient response in C.
975 elegans germline stem/progenitor cells. Development. 2012;139(5):859-70.
976 29. Roy D, Kahler DJ, Yun C, Hubbard EJA. Functional Interactions Between rsks-1/S6K, glp-
977 1/Notch, and Regulators of Caenorhabditis elegans Fertility and Germline Stem Cell
978 Maintenance. G3 (Bethesda). 2018;8(10):3293-309.
979 30. Fry AL, Webster AK, Burnett J, Chitrakar R, Baugh LR, Hubbard EJA. DAF-18/PTEN inhibits
980 germline zygotic gene activation during primordial germ cell quiescence. PLOS Genetics.
981 2021;17(7):e1009650.
982 31. Fukuyama M, Sakuma K, Park R, Kasuga H, Nagaya R, Atsumi Y, et al. C. elegans AMPKs
983 promote survival and arrest germline development during nutrient stress. Biology Open.
984 2012;1(10):929-36.
985 32. Demoinet E, Li S, Roy R. AMPK blocks starvation-inducible transgenerational defects in
986 Caenorhabditis elegans. Proc Natl Acad Sci U S A. 2017;114(13):E2689-e98.
987 33. Narbonne P, Maddox PS, Labbé J-C. DAF-18/PTEN signals through AAK-1/AMPK to
988 inhibit MPK-1/MAPK in feedback control of germline stem cell proliferation. PLOS Genetics.
989 2017;13(4):e1006738.
990 34. Masse I, Molin L, Billaud M, Solari F. Lifespan and dauer regulation by tissue-specific
991 activities of Caenorhabditis elegans DAF-18. Developmental Biology. 2005;286(1):91-101.
992 35. Tenen CC, Greenwald I. Cell Non-autonomous Function of daf-18/PTEN in the Somatic
993 Gonad Coordinates Somatic Gonad and Germline Development in C. elegans Dauer Larvae.
994 Current Biology. 2019;29(6):1064-72.e8.

995 36. Lee MH, Ohmachi M, Arur S, Nayak S, Francis R, Church D, et al. Multiple functions and
996 dynamic activation of MPK-1 extracellular signal-regulated kinase signaling in Caenorhabditis
997 elegans germline development. Genetics. 2007;177(4):2039-62.
998 37. Robinson-Thiewes S, Dufour B, Martel P-O, Lechasseur X, Brou AAD, Roy V, et al. Non-
999 autonomous regulation of germline stem cell proliferation by somatic MPK-1/MAPK activity in
1000 C. elegans. Cell Reports. 2021;35(8):109162.
1001 38. Church DL, Guan KL, Lambie EJ. Three genes of the MAP kinase cascade, mek-2, mpk-
1002 1/sur-1 and let-60 ras, are required for meiotic cell cycle progression in Caenorhabditis elegans.
1003 Development. 1995;121(8):2525-35.
1004 39. Miller MA, Nguyen VQ, Lee M-H, Kosinski M, Schedl T, Caprioli RM, Greenstein D. A
1005 Sperm Cytoskeletal Protein That Signals Oocyte Meiotic Maturation and Ovulation. Science.
1006 2001;291(5511):2144-7.
1007 40. Pinkston JM, Garigan D, Hansen M, Kenyon C. Mutations that increase the life span of C.
1008 elegans inhibit tumor growth. Science. 2006;313(5789):971-5.
1009 41. Killian DJ, Hubbard EJA. Caenorhabditis elegans germline patterning requires
1010 coordinated development of the somatic gonadal sheath and the germ line. Developmental
1011 Biology. 2005;279(2):322-35.
1012 42. Kimura KD, Tissenbaum HA, Liu Y, Ruvkun G. daf-2, an insulin receptor-like gene that
1013 regulates longevity and diapause in Caenorhabditis elegans. Science. 1997;277(5328):942-6.
1014 43. Swanson MM, Riddle DL. Critical periods in the development of the Caenorhabditis
1015 elegans dauer larva. Developmental Biology. 1981;84(1):27-40.
1016 44. Consortium CeDM. large-scale screening for targeted knockouts in the Caenorhabditis
1017 elegans genome. G3 (Bethesda). 2012;2(11):1415-25.
1018 45. Yen CA, Curran SP. Gene-diet interactions and aging in C. elegans. Exp Gerontol.
1019 2016;86:106-12.
1020 46. Murphy CT, Hu PJ. Insulin/insulin-like growth factor signaling in C. elegans. WormBook.
1021 2013:1-43.
1022 47. Mihaylova VT, Borland CZ, Manjarrez L, Stern MJ, Sun H. The PTEN tumor suppressor
1023 homolog in Caenorhabditis elegans regulates longevity and dauer formation in an insulin
1024 receptor-like signaling pathway. Proc Natl Acad Sci U S A. 1999;96(13):7427-32.
1025 48. Paradis S, Ruvkun G. Caenorhabditis elegans Akt/PKB transduces insulin receptor-like
1026 signals from AGE-1 PI3 kinase to the DAF-16 transcription factor. Genes Dev. 1998;12(16):2488-
1027 98.
1028 49. Lin K, Dorman JB, Rodan A, Kenyon C. daf-16: An HNF-3/forkhead Family Member
1029 That Can Function to Double the Life-Span of Caenorhabditis elegans. Science.
1030 1997;278(5341):1319-22.
1031 50. Lin K, Hsin H, Libina N, Kenyon C. Regulation of the Caenorhabditis elegans longevity
1032 protein DAF-16 by insulin/IGF-1 and germline signaling. Nat Genet. 2001;28(2):139-45.
1033 51. Lee RY, Hench J, Ruvkun G. Regulation of C. elegans DAF-16 and its human ortholog
1034 FKHRL1 by the daf-2 insulin-like signaling pathway. Curr Biol. 2001;11(24):1950-7.
1035 52. Henderson ST, Johnson TE. daf-16 integrates developmental and environmental inputs
1036 to mediate aging in the nematode Caenorhabditis elegans. Current Biology. 2001;11(24):1975-
1037 80.

1038 53. Aghayeva U, Bhattacharya A, Hobert O. A panel of fluorophore-tagged daf-16 alleles.
1039 MicroPubl Biol. 2020;2020.
1040 54. Zhang L, Ward JD, Cheng Z, Dernburg AF. The auxin-inducible degradation (AID) system
1041 enables versatile conditional protein depletion in C. elegans. Development. 2015;142(24):4374-
1042 84.
1043 55. Zhang YP, Zhang WH, Zhang P, Li Q, Sun Y, Wang JW, et al. Intestine-specific removal of
1044 DAF-2 nearly doubles lifespan in Caenorhabditis elegans with little fitness cost. Nat Commun.
1045 2022;13(1):6339.
1046 56. Zou L, Wu D, Zang X, Wang Z, Wu Z, Chen D. Construction of a germline-specific RNAi
1047 tool in C. elegans. Scientific Reports. 2019;9(1):2354.
1048 57. Lara-Gonzalez P, Moyle MW, Budrewicz J, Mendoza-Lopez J, Oegema K, Desai A. The G2-
1049 to-M Transition Is Ensured by a Dual Mechanism that Protects Cyclin B from Degradation by
1050 Cdc20-Activated APC/C. Dev Cell. 2019;51(3):313-25.e10.
1051 58. Tarailo-Graovac M, Wang J, Chu JSC, Tu D, Baillie DL, Chen N. Spindle assembly
1052 checkpoint genes reveal distinct as well as overlapping expression that implicates MDF-2/Mad2
1053 in postembryonic seam cell proliferation in Caenorhabditis elegans. BMC Cell Biology.
1054 2010;11(1):71.
1055 59. Gartner A, Milstein S, Ahmed S, Hodgkin J, Hengartner MO. A conserved checkpoint
1056 pathway mediates DNA damage--induced apoptosis and cell cycle arrest in C. elegans. Mol Cell.
1057 2000;5(3):435-43.
1058 60. Raiders SA, Eastwood MD, Bacher M, Priess JR. Binucleate germ cells in Caenorhabditis
1059 elegans are removed by physiological apoptosis. PLoS Genet. 2018;14(7):e1007417.
1060 61. Stevens D, Oegema K, Desai A. Meiotic double-strand breaks uncover and protect
1061 against mitotic errors in the C. elegans germline. Curr Biol. 2013;23(23):2400-6.
1062 62. Greer EL, Dowlatshahi D, Banko MR, Villen J, Hoang K, Blanchard D, et al. An AMPK-
1063 FOXO pathway mediates longevity induced by a novel method of dietary restriction in C.
1064 elegans. Curr Biol. 2007;17(19):1646-56.
1065 63. Avery L. The genetics of feeding in Caenorhabditis elegans. Genetics. 1993;133(4):897-
1066 917.
1067 64. Narbonne P, Roy R. Caenorhabditis elegans dauers need LKB1/AMPK to ration lipid
1068 reserves and ensure long-term survival. Nature. 2009;457(7226):210-4.
1069 65. Apfeld J, O'Connor G, McDonagh T, DiStefano PS, Curtis R. The AMP-activated protein
1070 kinase AAK-2 links energy levels and insulin-like signals to lifespan in C. elegans. Genes Dev.
1071 2004;18(24):3004-9.
1072 66. Roy D, Michaelson D, Hochman T, Santella A, Bao Z, Goldberg JD, Hubbard EJA. Cell cycle
1073 features of C. elegans germline stem/progenitor cells vary temporally and spatially.
1074 Developmental Biology. 2016;409(1):261-71.
1075 67. Hardie DG, Ross FA, Hawley SA. AMPK: a nutrient and energy sensor that maintains
1076 energy homeostasis. Nature Reviews Molecular Cell Biology. 2012;13(4):251-62.
1077 68. Banko MR, Allen JJ, Schaffer BE, Wilker EW, Tsou P, White JL, et al. Chemical genetic
1078 screen for AMPKα2 substrates uncovers a network of proteins involved in mitosis. Mol Cell.
1079 2011;44(6):878-92.
1080 69. Lee JH, Koh H, Kim M, Kim Y, Lee SY, Karess RE, et al. Energy-dependent regulation of
1081 cell structure by AMP-activated protein kinase. Nature. 2007;447(7147):1017-20.

1082 70. Vazquez-Martin A, Oliveras-Ferraros C, Menendez JA. The active form of the metabolic
1083 sensor: AMP-activated protein kinase (AMPK) directly binds the mitotic apparatus and travels
1084 from centrosomes to the spindle midzone during mitosis and cytokinesis. Cell Cycle.
1085 2009;8(15):2385-98.
1086 71. Zhao H, Li T, Wang K, Zhao F, Chen J, Xu G, et al. AMPK-mediated activation of MCU
1087 stimulates mitochondrial Ca(2+) entry to promote mitotic progression. Nat Cell Biol.
1088 2019;21(4):476-86.
1089 72. Pines J. Mitosis: a matter of getting rid of the right protein at the right time. Trends Cell
1090 Biol. 2006;16(1):55-63.
1091 73. Collin P, Nashchekina O, Walker R, Pines J. The spindle assembly checkpoint works like a
1092 rheostat rather than a toggle switch. Nat Cell Biol. 2013;15(11):1378-85.
1093 74. London N, Biggins S. Signalling dynamics in the spindle checkpoint response. Nat Rev
1094 Mol Cell Biol. 2014;15(11):736-47.
1095 75. Dudka D, Noatynska A, Smith CA, Liaudet N, McAinsh AD, Meraldi P. Complete
1096 microtubule–kinetochore occupancy favours the segregation of merotelic attachments. Nature
1097 Communications. 2018;9(1):2042.
1098 76. Etemad B, Vertesy A, Kuijt TEF, Sacristan C, van Oudenaarden A, Kops G. Spindle
1099 checkpoint silencing at kinetochores with submaximal microtubule occupancy. J Cell Sci.
1100 2019;132(12).
1101 77. Kuhn J, Dumont S. Spindle assembly checkpoint satisfaction occurs via end-on but not
1102 lateral attachments under tension. J Cell Biol. 2017;216(6):1533-42.
1103 78. Kuhn J, Dumont S. Mammalian kinetochores count attached microtubules in a sensitive
1104 and switch-like manner. J Cell Biol. 2019;218(11):3583-96.
1105 79. McAinsh AD, Kops GJPL. Principles and dynamics of spindle assembly checkpoint
1106 signalling. Nature Reviews Molecular Cell Biology. 2023;24(8):543-59.
1107 80. Foster SA, Morgan DO. The APC/C subunit Mnd2/Apc15 promotes Cdc20
1108 autoubiquitination and spindle assembly checkpoint inactivation. Mol Cell. 2012;47(6):921-32.
1109 81. Kim DH, Han JS, Ly P, Ye Q, McMahon MA, Myung K, et al. TRIP13 and APC15 drive
1110 mitotic exit by turnover of interphase- and unattached kinetochore-produced MCC. Nat
1111 Commun. 2018;9(1):4354.
1112 82. Ma HT, Chan YY, Chen X, On KF, Poon RY. Depletion of p31comet protein promotes
1113 sensitivity to antimitotic drugs. J Biol Chem. 2012;287(25):21561-9.
1114 83. Mansfeld J, Collin P, Collins MO, Choudhary JS, Pines J. APC15 drives the turnover of
1115 MCC-CDC20 to make the spindle assembly checkpoint responsive to kinetochore attachment.
1116 Nat Cell Biol. 2011;13(10):1234-43.
1117 84. Uzunova K, Dye BT, Schutz H, Ladurner R, Petzold G, Toyoda Y, et al. APC15 mediates
1118 CDC20 autoubiquitylation by APC/C(MCC) and disassembly of the mitotic checkpoint complex.
1119 Nat Struct Mol Biol. 2012;19(11):1116-23.
1120 85. Westhorpe FG, Tighe A, Lara-Gonzalez P, Taylor SS. p31comet-mediated extraction of
1121 Mad2 from the MCC promotes efficient mitotic exit. J Cell Sci. 2011;124(Pt 22):3905-16.
1122 86. Ye Q, Rosenberg SC, Moeller A, Speir JA, Su TY, Corbett KD. TRIP13 is a protein-
1123 remodeling AAA+ ATPase that catalyzes MAD2 conformation switching. Elife. 2015;4.

1124 87. Murphy CT, Lee SJ, Kenyon C. Tissue entrainment by feedback regulation of insulin gene
1125 expression in the endoderm of Caenorhabditis elegans. Proc Natl Acad Sci U S A.
1126 2007;104(48):19046-50.
1127 88. Murphy CT, McCarroll SA, Bargmann CI, Fraser A, Kamath RS, Ahringer J, et al. Genes
1128 that act downstream of DAF-16 to influence the lifespan of Caenorhabditis elegans. Nature.
1129 2003;424(6946):277-83.
1130 89. Aghayeva U, Bhattacharya A, Sural S, Jaeger E, Churgin M, Fang-Yen C, Hobert O. DAF-
1131 16/FoxO and DAF-12/VDR control cellular plasticity both cell-autonomously and via interorgan
1132 signaling. PLOS Biology. 2021;19(4):e3001204.
1133 90. Zhang P, Judy M, Lee S-J, Kenyon C. Direct and Indirect Gene Regulation by a Life-
1134 Extending FOXO Protein in C. elegans: Roles for GATA Factors and Lipid Gene Regulators. Cell
1135 Metabolism. 2013;17(1):85-100.
1136 91. Laoukili J, Kooistra MR, Bras A, Kauw J, Kerkhoven RM, Morrison A, et al. FoxM1 is
1137 required for execution of the mitotic programme and chromosome stability. Nat Cell Biol.
1138 2005;7(2):126-36.
1139 92. Zhu G, Spellman PT, Volpe T, Brown PO, Botstein D, Davis TN, Futcher B. Two yeast
1140 forkhead genes regulate the cell cycle and pseudohyphal growth. Nature. 2000;406(6791):90-4.
1141 93. Ewe CK, Alok G, Rothman JH. Stressful development: integrating endoderm
1142 development, stress, and longevity. Developmental Biology. 2021;471:34-48.
1143 94. Killian DJ, Hubbard EJA. C. elegans pro-1 activity is required for soma/germline
1144 interactions that influence proliferation and differentiation in the germ line. Development.
1145 2004;131(6):1267-78.
1146 95. McCarter J, Bartlett B, Dang T, Schedl T. Soma–Germ Cell Interactions inCaenorhabditis
1147 elegans:Multiple Events of Hermaphrodite Germline Development Require the Somatic Sheath
1148 and Spermathecal Lineages. Developmental Biology. 1997;181(2):121-43.
1149 96. Starich TA, Hall DH, Greenstein D. Two classes of gap junction channels mediate soma-
1150 germline interactions essential for germline proliferation and gametogenesis in Caenorhabditis
1151 elegans. Genetics. 2014;198(3):1127-53.
1152 97. Hall DH, Winfrey VP, Blaeuer G, Hoffman LH, Furuta T, Rose KL, et al. Ultrastructural
1153 features of the adult hermaphrodite gonad of Caenorhabditis elegans: relations between the
1154 germ line and soma. Dev Biol. 1999;212(1):101-23.
1155 98. Brenner S. The genetics of Caenorhabditis elegans. Genetics. 1974;77(1):71-94.
1156 99. Chaudhari SN, Mukherjee M, Vagasi AS, Bi G, Rahman MM, Nguyen CQ, et al. Bacterial
1157 Folates Provide an Exogenous Signal for C. elegans Germline Stem Cell Proliferation. Dev Cell.
1158 2016;38(1):33-46.
1159 100. Stiernagle T. Maintenance of *C. elegans*. WormBook: The Online Review of C elegans
1160 Biology. Pasadena (CA)2006.
1161 101. Martinez MAQ, Matus DQ. Auxin-mediated Protein Degradation in Caenorhabditis
1162 elegans. Bio Protoc. 2020;10(8).
1163 102. Negishi T, Kitagawa S, Horii N, Tanaka Y, Haruta N, Sugimoto A, et al. The auxin-inducible
1164 degron 2 (AID2) system enables controlled protein knockdown during embryogenesis and
1165 development in Caenorhabditis elegans. Genetics. 2022;220(2).
1166 103. Schiksnis E, Nicholson A, Modena M, Pule M, Arribere J, Pasquinelli A. Auxin-
1167 independent depletion of degron-tagged proteins by TIR1. MicroPubl Biol. 2020;2020.

1168 104. Kamath RS, Martinez-Campos M, Zipperlen P, Fraser AG, Ahringer J. Effectiveness of
1169 specific RNA-mediated interference through ingested double-stranded RNA in Caenorhabditis
1170 elegans. Genome Biol. 2001;2(1):Research0002.
1171 105. Schindelin J, Arganda-Carreras I, Frise E, Kaynig V, Longair M, Pietzsch T, et al. Fiji: an
1172 open-source platform for biological-image analysis. Nat Methods. 2012;9(7):676-82.
1173 106. Tinevez JY, Perry N, Schindelin J, Hoopes GM, Reynolds GD, Laplantine E, et al.
1174 TrackMate: An open and extensible platform for single-particle tracking. Methods.
1175 2017;115:80-90.
1176 107. Ershov D, Phan MS, Pylvänäinen JW, Rigaud SU, Le Blanc L, Charles-Orszag A, et al.
1177 TrackMate 7: integrating state-of-the-art segmentation algorithms into tracking pipelines. Nat
1178 Methods. 2022;19(7):829-32.
1179 108. Hansen D, Albert Hubbard EJ, Schedl T. Multi-pathway control of the proliferation versus
1180 meiotic development decision in the Caenorhabditis elegans germline. Developmental Biology.
1181 2004;268(2):342-57.
1182 109. MacQueen AJ, Villeneuve AM. Nuclear reorganization and homologous chromosome
1183 pairing during meiotic prophase require C. elegans chk-2. Genes & Development.
1184 2001;15(13):1674-87.
1185 110. Zhou Z, Hartwieg E, Horvitz HR. CED-1 Is a Transmembrane Receptor that Mediates Cell
1186 Corpse Engulfment in C. elegans. Cell. 2001;104(1):43-56.
1187 111. Sternberg PW, Van Auken K, Wang Q, Wright A, Yook K, Zarowiecki M, et al. WormBase
1188 2024: status and transitioning to Alliance infrastructure. Genetics. 2024;227(1).
1189

Figure 1

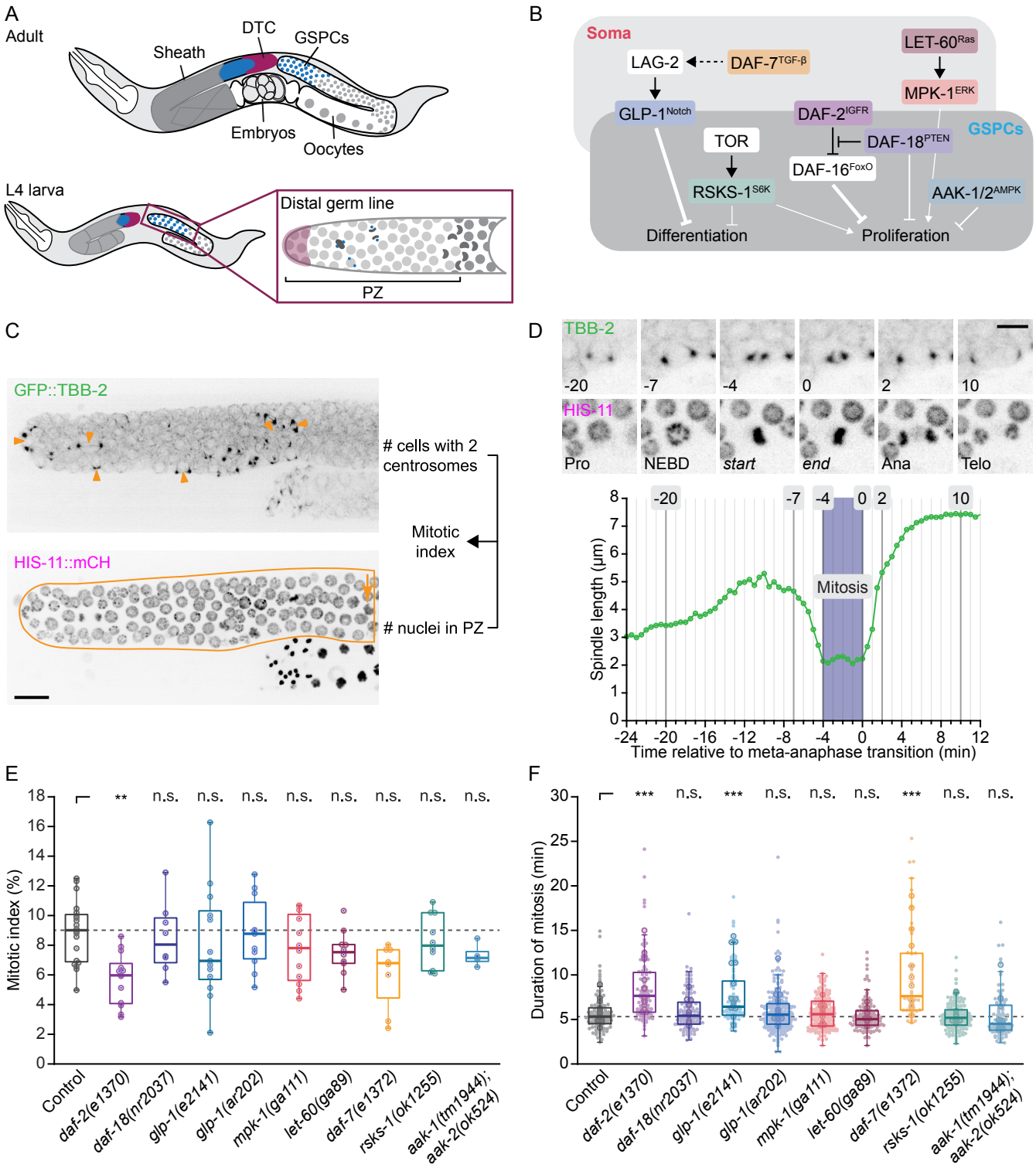
A
Adult
Sheath
DTC
GSPCs
Embryos
Oocytes
L4 larva
Distal germ line
PZ
B
Soma
LAG-2
DAF-7TGF-β
LET-60Ras
MPK-1ERK
GLP-1Notch
DAF-2IGFR
GSPCs
TOR
DAF-18PTEN
DAF-16FoxO
RSKS-1S6K
AAK-1/2AMPK
Differentiation
Proliferation
C
GFP::TBB-2
cells with 2 centrosomes
Mitotic index
HIS-11::mCH
nuclei in PZ
D
TBB-2
-20
-7
-4
0
2
10
HIS-11
Pro
NEBD
start
end
Ana
Telo
Spindle length (µm)
Mitosis
Time relative to meta-anaphase transition (min)
E
Mitotic index (%)
**
n.s.
Control
daf-2(e1370)
daf-18(nr2037)
glp-1(e2141)
glp-1(ar202)
mpk-1(ga111)
let-60(ga89)
daf-7(e1372)
rsks-1(ok1255)
aak-1(tm1944); aak-2(ok524)
F
Duration of mitosis (min)
***
n.s.

Figure 2

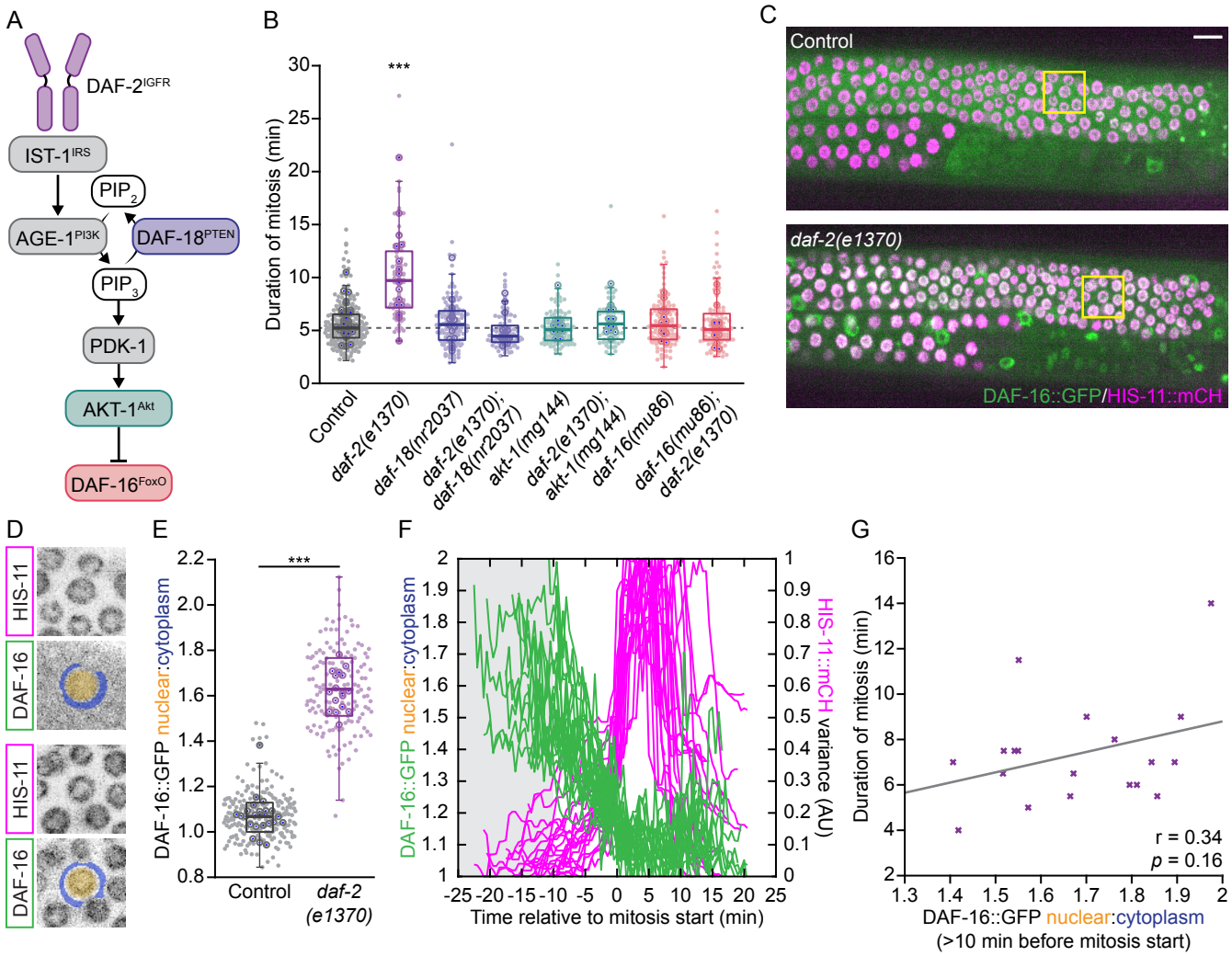
A
DAF-2IGFR
IST-1IRS
PIP2
AGE-1PI3K
DAF-18PTEN
PIP3
PDK-1
AKT-1Akt
DAF-16FoxO
B
Duration of mitosis (min)
***
Control
daf-2(e1370)
daf-18(nr2037)
daf-2(e1370); daf-18(nr2037)
akt-1(mg144)
daf-2(e1370); akt-1(mg144)
daf-16(mu86)
daf-16(mu86); daf-2(e1370)
C
Control
daf-2(e1370)
DAF-16::GFP/HIS-11::mCH
D
HIS-11
DAF-16
HIS-11
DAF-16
E
DAF-16::GFP nuclear:cytoplasm
***
Control
daf-2 (e1370)
F
DAF-16::GFP nuclear:cytoplasm
HIS-11::mCH variance (AU)
Time relative to mitosis start (min)
G
Duration of mitosis (min)
r = 0.34
p = 0.16
DAF-16::GFP nuclear:cytoplasm
(>10 min before mitosis start)

Figure 3

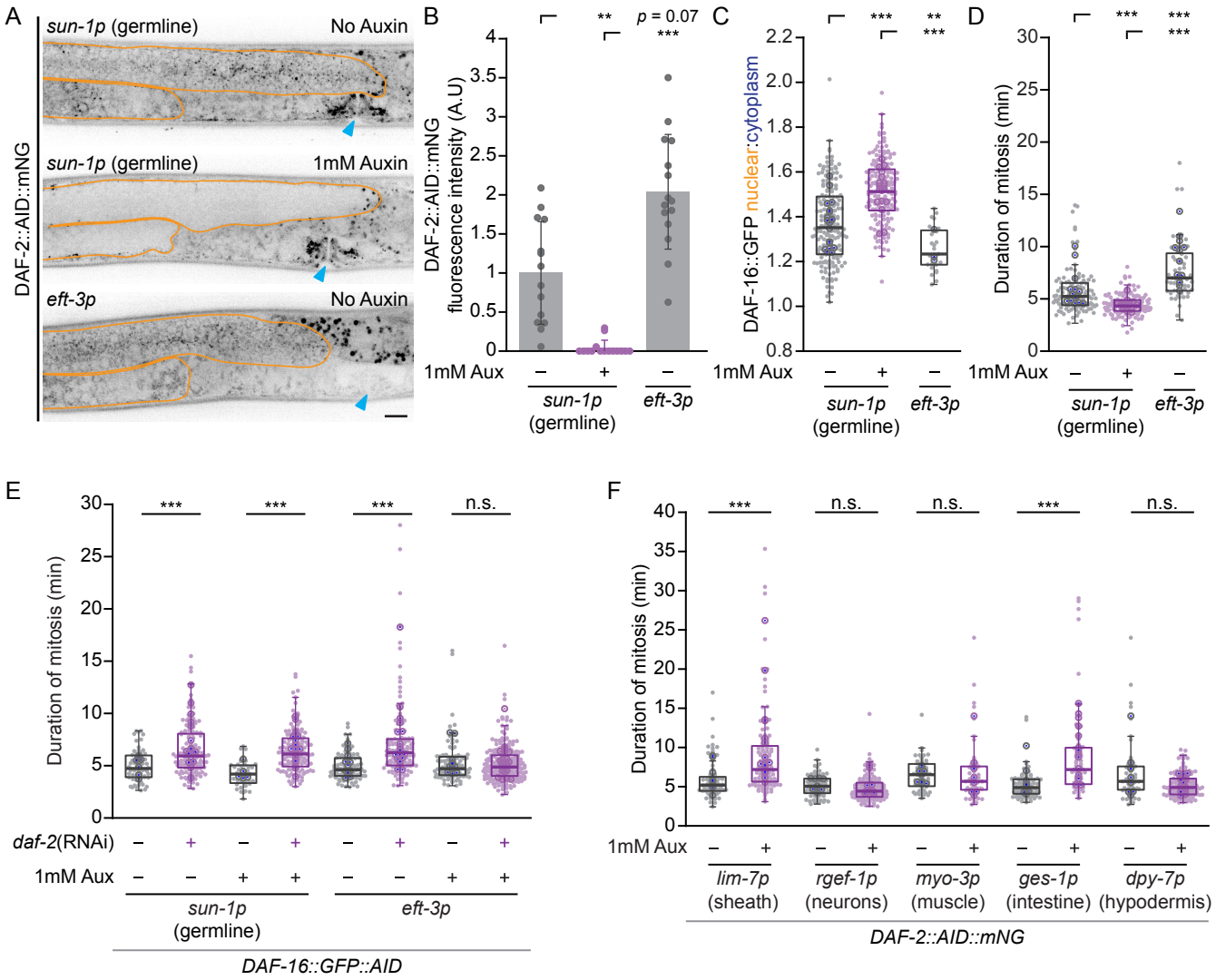
A
sun-1p (germline)
No Auxin
sun-1p (germline)
1mM Auxin
eft-3p
No Auxin
DAF-2::AID::mNG
B
DAF-2::AID::mNG fluorescence intensity (A.U)
p = 0.07
1mM Aux
sun-1p (germline)
eft-3p
C
DAF-16::GFP nuclear:cytoplasm
1mM Aux
sun-1p (germline)
eft-3p
D
Duration of mitosis (min)
1mM Aux
sun-1p (germline)
eft-3p
E
Duration of mitosis (min)
daf-2(RNAi)
1mM Aux
sun-1p (germline)
eft-3p
DAF-16::GFP::AID
n.s.
F
Duration of mitosis (min)
1mM Aux
lim-7p (sheath)
rgef-1p (neurons)
myo-3p (muscle)
ges-1p (intestine)
dpy-7p (hypodermis)
DAF-2::AID::mNG

Figure 4

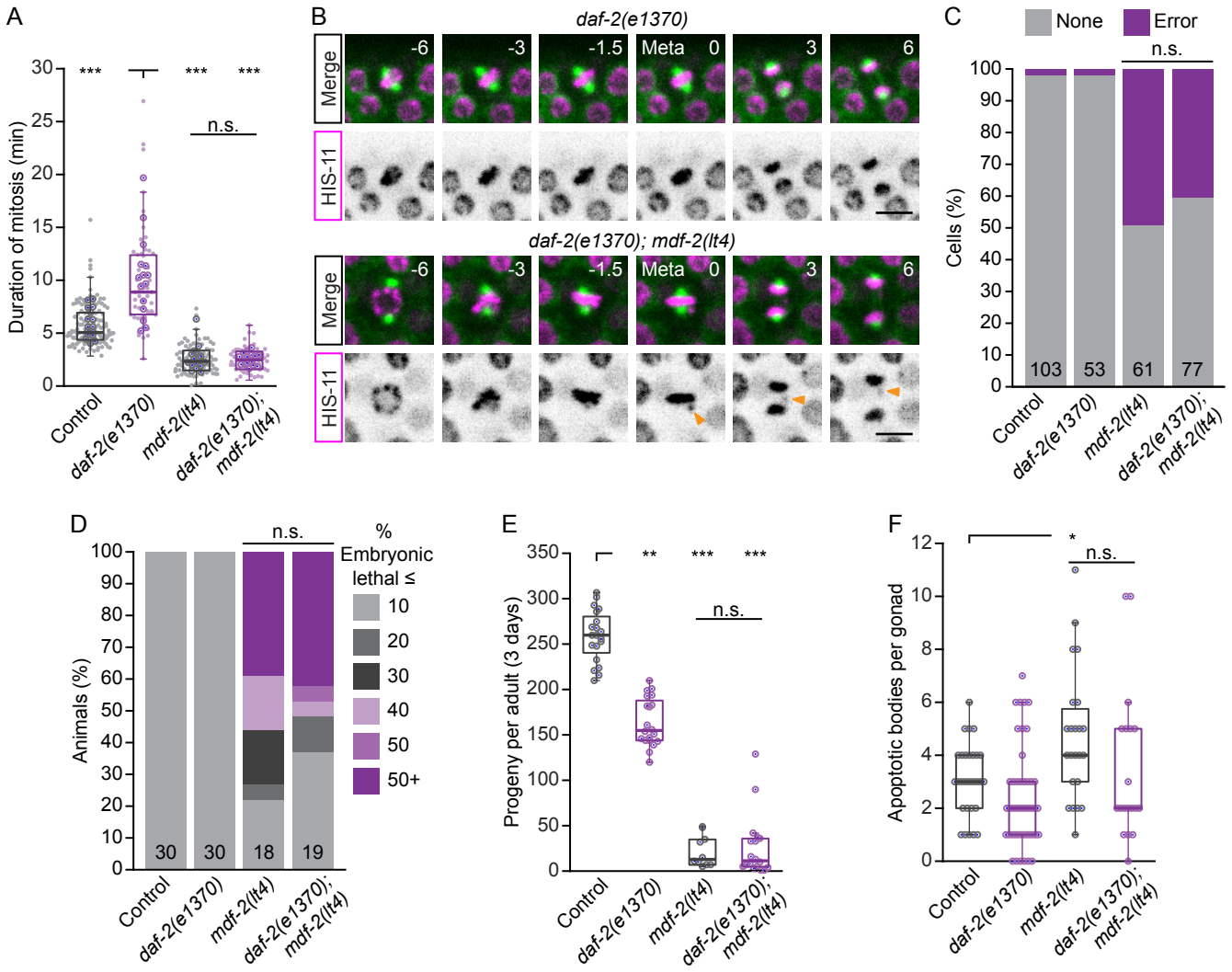
A
Duration of mitosis (min)
***
***
***
n.s.
Control
daf-2(e1370)
mdf-2(lt4)
daf-2(e1370); mdf-2(lt4)
B
daf-2(e1370)
Merge
HIS-11
-6
-3
-1.5
Meta
0
3
6
daf-2(e1370); mdf-2(lt4)
C
None
Error
n.s.
Cells (%)
103
53
61
77
D
n.s.
Animals (%)
% Embryonic lethal ≤
10
20
30
40
50
50+
30
30
18
19
E
Progeny per adult (3 days)
**
***
***
n.s.
F
Apoptotic bodies per gonad
*
n.s.

Figure 5

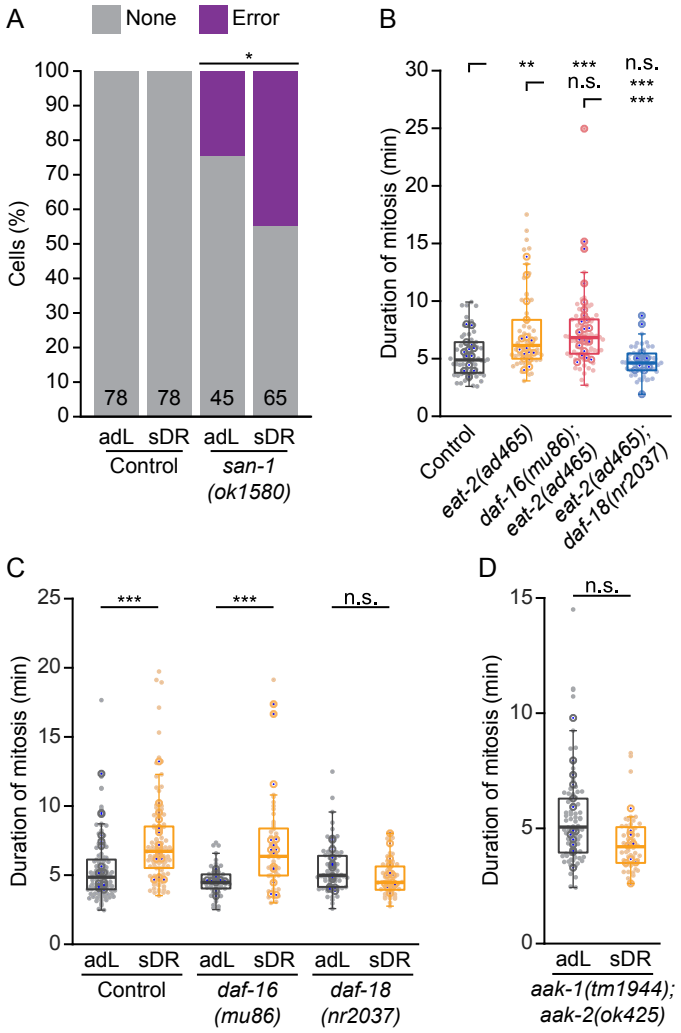
A
None
Error
Cells (%)
100
90
80
70
60
50
40
30
20
10
0
*
78
78
45
65
adL
sDR
adL
sDR
Control
san-1
(ok1580)
B
Duration of mitosis (min)
30
25
20
15
10
5
0
**
***
n.s.
n.s.
***
***
Control
eat-2(ad465)
daf-16(mu86);
eat-2(ad465)
eat-2(ad465);
daf-18(nr2037)
C
Duration of mitosis (min)
25
20
15
10
5
0
***
***
n.s.
adL
sDR
adL
sDR
adL
sDR
Control
daf-16
(mu86)
daf-18
(nr2037)
D
Duration of mitosis (min)
15
10
5
0
n.s.
adL
sDR
aak-1(tm1944);
aak-2(ok425)